Journal of Computational Physics 341 (2017) 22–43

Contents lists available at ScienceDirect

Journal of Computational Physics

www.elsevier.com/locate/jcp

A weighted multiple-relaxation-time lattice Boltzmann method for multiphase flows and its application to partial coalescence cascades

Abbas Fakhari [a,*], Diogo Bolster [a], Li-Shi Luo [b,c]

[a] Department of Civil and Environmental Engineering and Earth Sciences, University of Notre Dame, Notre Dame, IN 46556, USA
[b] Computational Science Research Center, Beijing 100193, China
[c] Department of Mathematics and Statistics, Old Dominion University, Norfolk, VA 23529, USA

ARTICLE INFO

Article history:
Received 21 April 2016
Received in revised form 22 February 2017
Accepted 31 March 2017
Available online 4 April 2017

Keywords:
Multiphase flow
Interfacial dynamics
Partial coalescence
Coalescence cascade
Lattice Boltzmann method
Adaptive mesh refinement

ABSTRACT

We present a lattice Boltzmann method (LBM) with a weighted multiple-relaxation-time (WMRT) collision model and an adaptive mesh refinement (AMR) algorithm for direct numerical simulation of two-phase flows in three dimensions. The proposed WMRT model enhances the numerical stability of the LBM for immiscible fluids at high density ratios, particularly on the D3Q27 lattice. The effectiveness and efficiency of the proposed WMRT–LBM–AMR is validated through simulations of (a) buoyancy-driven motion and deformation of a gas bubble rising in a viscous liquid; (b) the bag-breakup mechanism of a falling drop; (c) crown splashing of a droplet on a wet surface; and (d) the partial coalescence mechanism of a liquid drop at a liquid–liquid interface. The numerical simulations agree well with available experimental data and theoretical approximations where applicable.

1. Introduction

Reliable simulation of multiphase flows under stiff conditions, which could be due to large Reynolds number and/or high density ratios, remains a challenge in computational fluid dynamics (CFD). Sharp-interface methods and their counterparts, diffuse-interface methods, are two distinct approaches for modeling interfacial dynamics [1]. Existing methods based on these techniques differ in terms of accuracy, efficiency, and ease of implementation. In this work, a particular subclass of diffuse-interface method, namely phase-field modeling, will be considered. In the phase-field approach, an advection–diffusion-type equation, based on either Cahn–Hilliard [2] or Allen–Cahn [3] models, is used to track interfaces, which are assumed to have a finite thickness as opposed to zero-thickness in sharp-interface methods. In this study, we use the lattice Boltzmann equation (LBE) [4,5] to solve the governing equations for multiphase flows.

As opposed to traditional CFD methods based on some direct discretization of the Navier–Stokes equations, the LBE is derived from kinetic theory [6,7]. In lattice Boltzmann methods (LBM), the LBE solves the conservation laws based on linearized kinetic models. In this work we use the LBE with a multiple-relaxation-time (MRT) collision model [8–10], which is far more effective, in terms of numerical stability and accuracy [10], than the single-relaxation-time (SRT) collision model, also known as the lattice Bhatnagar–Gross–Krook (LBGK) model [11,12]. The MRT–LBE approach is based on projection theory: the advection process of the particle distribution function is carried out in the particle velocity space, whereas the collision process is done in moment space, i.e., the distribution function is projected to its velocity moments during

* Corresponding author.
E-mail addresses: afakhari@nd.edu (A. Fakhari), dbolster@nd.edu (D. Bolster), lluo@odu.edu (L.-S. Luo).

http://dx.doi.org/10.1016/j.jcp.2017.03.062
0021-9991/

the collision process. Because the moments include some physical observables, such as the flow density, momentum, and energy, as well as their fluxes, the relaxation processes of the moments are physically meaningful; the relaxation of stresses is related to viscous dissipation of the momentum whereas the relaxation of the heat fluxes is related to thermal dissipation. With the MRT collision model, all transport coefficients for different processes can be tuned independently, as opposed to the LBGK model, in which all dissipation coefficients are identical as they are determined by the only relaxation parameter in the model. With the maximum degrees of freedom in utilizing all relaxation rates theoretically allowed in a lattice Boltzmann (LB) model, the MRT model not only optimizes the numerical efficiency of the LBE [9,10], it also removes the inherent defect of the LBGK model in treating boundary conditions [13].

Traditionally, the moments in the MRT–LBE are those of the particle velocity, and they are mutually orthogonal on the discrete velocity set $\{\boldsymbol{c}_i\}$ with a uniform weight function of unity [8–10]. This formulation leads to some undesirable coupling between the conserved hydrodynamic moments, i.e., flow density ρ, and some higher-order, non-hydrodynamic ones [14,15], which do not exist in the continuous velocity space. In particular, the most conspicuous spurious coupling is between the density and the forth-order moment. These spurious couplings can affect numerical stability in LB simulations. Some of these couplings can be removed by orthogonalization of moments with a non-uniform weight function [14], resulting in a weighed MRT (WMRT) model. In this work, the WMRT model in 2D [14] will be extended to 3D with 15, 19, and 27 discrete velocities.

A major computational challenge in simulation of multiphase flows is the requirement to adequately resolve the interfacial region between different fluids. This necessitates high resolution in the vicinity of the interface. A uniform grid throughout the entire computational domain is inefficient and may be too costly in terms of computational resources. Techniques based on adaptive mesh refinement (AMR) algorithms are very effective in tackling this issue [16–21]. While AMR techniques have been used with LBM previously [22–27], only recently, a new AMR–MRT–LBM for two-phase flows in 2D was developed [28] using a conservative phase-field LBE [29] and an MRT–LBM for immiscible two-phase flows [30].

In this work, we develop 3D WMRT–LB models with enhanced numerical stability and robustness. With the conventional notation DdQq to denote an LB model in d dimensions with q discrete velocities, we develop D3Q15, D3Q19, and D3Q27 WMRT–LB models. We also extend our previously proposed AMR algorithm [28] from 2D to 3D. We then consolidate the proposed WMRT–LBM and AMR to construct an efficient AMR–LBM for direct numerical simulation of multiphase flows in 3D. Given that the proposed AMR algorithm, particularly in 3D, could be rather complicated and beyond the scope of interest for some people, we will formulate a stand-alone WMRT–LBM in such a way that interested readers are able to fully exploit the proposed model without having to use the AMR routine.

To demonstrate the effectiveness and efficiency of our proposed AMR–LBM for multiphase flows, we selectively study a few challenging interfacial phenomena in droplet and bubble dynamics [31]. We first consider three interesting test problems: (a) the buoyancy-driven motion of a rising bubble [32]; (b) a falling droplet [33], and (c) the splashing of a drop on a wet surface [34]. Then, we focus on one particularly challenging problem: a droplet coalescing with a flat liquid pool and the mechanism of partial coalescence [35].

In partial coalescence, a drop partially merges with a liquid interface, and instead of a complete coalescence, a daughter droplet of smaller size is left behind. The dynamics of partial coalescence of a liquid drop at a liquid–liquid interface have been studied by many previously [35–41]. The pioneering experiments of Charles and Mason [35] reported as many as eight consecutive stages of observable partial coalescence at a liquid–liquid interface. Thoroddsen and Takehara [36] observed up to six stages in the coalescence cascade between a liquid drop and a liquid–air interface. Subsequent experimental and numerical studies demonstrate the importance of viscous, inertial, buoyancy and surface tension forces [38,39,41]. All aforementioned studies observe secondary droplets produced at small values of the Ohnesorge number, which quantifies the relative strength of viscous force over interfacial tension. Consequently, the governing equations become stiff due to either a large Reynolds number or a small Weber number. Thus, it is numerically challenging to simulate interfacial dynamics at small Ohnesorge numbers. To the best of our knowledge, all numerical simulations of partial coalescence at a flat liquid–liquid interface to date are carried out in axisymmetric coordinates [37,39,41]. Given that non-axisymmetric perturbations can grow and become significant at high Reynolds numbers (corresponding to low Ohnesorge numbers), genuine 3D simulations are invaluable in studying these phenomena. Therefore, the partial coalescence phenomenon will be revisited in this study by using the proposed WMRT–LBM with AMR in 3D.

The remainder of this paper is organized as follows. In Sec. 2 we present the formulation of the conservative phase-field LBE for interface tracking. We describe the 3D WMRT–LBM that recovers the Navier–Stokes equations in Sec. 3. In Sec. 4 we discuss the numerical implementation of the proposed model. In Sec. 5 we present numerical results for three benchmark studies: (a) an air bubble rising due to buoyancy, (b) breakup of a falling liquid drop under gravity, and (c) droplet splashing onto a wet surface. We investigate the partial coalescence mechanism of a liquid drop at a liquid–liquid interface in Sec. 6. Section 7 summarizes the paper, and (Appendix A) provides the technical details of constructing WMRT models for D3Q15, D3Q19, and D3Q27 lattices. This includes the weight coefficients and the transformation matrices, which map the distribution function to its moments.

2. Conservative phase-field LBE

We consider a two-phase system with light and heavy fluids, and define the phase-field variable ϕ such that it is zero in one phase (light fluid) and one in the other (heavy fluid). Most phase-field-based LB models mimic the Cahn–Hilliard

equation [42]. From the numerical viewpoint, an undesirable feature of the Cahn–Hilliard model is the need to calculate the Laplacian of the chemical potential, which implies computation of a fourth-order derivative. This shortcoming is reduced to the calculation of second-order derivatives in the phase-field model proposed by Sun and Beckermann [43]. This can be further reduced to the calculation of first-order derivatives using LBM [29].

The conservative phase-field equation for interface tracking in incompressible binary fluids can be written as [44]

$$\frac{\partial \phi}{\partial t} + \nabla \cdot (\phi \boldsymbol{u}) = \nabla \cdot \left[M \left(\nabla \phi - \frac{4}{\xi} \phi (1-\phi) \hat{\boldsymbol{n}} \right) \right], \tag{1}$$

where t stands for time, $\boldsymbol{u}$ is the macroscopic velocity vector, M is the mobility and ξ is the interface thickness (see Sec. 6.2 for a practical guideline on choosing these parameters), and $\hat{\boldsymbol{n}}$ is the unit vector out-normal to the interface

$$\hat{\boldsymbol{n}} = \frac{\nabla \phi}{|\nabla \phi|} \tag{2}$$

(see Eq. (33) and the following paragraph for numerical implementation of $\hat{\boldsymbol{n}}$). For an interface located at $\boldsymbol{r}_0$ and at thermodynamic equilibrium, the phase-field distribution at $\boldsymbol{r}$ assumes a hyperbolic tangent profile

$$\phi(\boldsymbol{r}) = \frac{1}{2} \left[1 \pm \tanh \left(\frac{2|\boldsymbol{r} - \boldsymbol{r}_0|}{\xi} \right) \right]. \tag{3}$$

In order to recover phase-field equation (1), the following LBE is proposed [29]:

$$\frac{\partial h_i}{\partial t} + \boldsymbol{c}_i \cdot \nabla h_i = -\frac{h_i - h_i^{(\mathrm{eq})}}{\lambda_\phi}, \tag{4}$$

where h_i is the phase-field distribution function, λ_ϕ is the phase-field relaxation rate, and $\boldsymbol{c}_i$ ($i = 0, 1, 2, \ldots, q-1$) is the microscopic velocity set which is given in Appendix A for different lattices in 3D. The equilibrium phase-field distribution function is [29]

$$h_i^{(\mathrm{eq})} = \phi \Gamma_i + w_i \frac{M}{c_s^2} \left[\frac{4}{\xi} \phi (1-\phi) \right] (\boldsymbol{c}_i \cdot \hat{\boldsymbol{n}}), \tag{5}$$

in which

$$\Gamma_i = w_i \left[1 + \frac{\boldsymbol{c}_i \cdot \boldsymbol{u}}{c_s^2} + \frac{1}{2} \left(\frac{\boldsymbol{c}_i \boldsymbol{c}_i}{c_s^2} - \mathbf{I} \right) : \frac{\boldsymbol{u}\boldsymbol{u}}{c_s^2} \right], \tag{6}$$

where $c_s = c/\sqrt{3}$ is the speed of sound in the system, $c = \delta x/\delta t$ (for uniform grids $\delta x = \delta t = 1$ lu (lattice units)), $\mathbf{I}$ is the $d \times d$ identity matrix in which d is the spatial dimension, and w_i is the weight coefficient set corresponding to the velocity set $\boldsymbol{c}_i$ [7] (see Appendix A). The mobility is related to the phase-field relaxation rate by

$$M = \lambda_\phi c_s^2. \tag{7}$$

The phase-field LBE (4) can be solved in two steps:

$$\text{collision:} \qquad h_i^*(\boldsymbol{x}, t) = h_i(\boldsymbol{x}, t) + \boldsymbol{\Omega}_h, \tag{8a}$$

$$\text{advection:} \qquad \frac{\partial h_i^*}{\partial t} + \boldsymbol{c}_i \cdot \nabla h_i^* = 0, \tag{8b}$$

where h_i^* denotes the post-collision value of h_i and $\boldsymbol{\Omega}_h = -(h_i - h_i^{(\mathrm{eq})})/\tau_\phi$ is the collision operator where $\tau_\phi = \lambda_\phi/\delta t + 1/2$. On uniform grids, perfect shift $h_i(\boldsymbol{x}, t+\delta t) = h_i^*(\boldsymbol{x} - \boldsymbol{c}_i \delta t, t)$ is the exact solution to the advection equation; therefore, the following relation holds when $\delta x = \delta t$:

$$h_i(\boldsymbol{x} + \boldsymbol{c}_i \delta t, t + \delta t) = h_i(\boldsymbol{x}, t) - \frac{h_i(\boldsymbol{x}, t) - h_i^{(\mathrm{eq})}(\boldsymbol{x}, t)}{\tau_\phi}. \tag{9}$$

The phase field is then calculated by taking the zeroth moment of the phase-field distribution function

$$\phi = \sum_{i=0}^{q-1} h_i \tag{10}$$

and the density ρ is simply found by a linear interpolation

$$\rho = \rho_\mathrm{L} + (\rho_\mathrm{H} - \rho_\mathrm{L}) \phi, \tag{11}$$

where ρ_L and ρ_H are the bulk densities of the light and heavy fluids, respectively.

3. LBE for pressure evolution

The discrete Boltzmann equation for the particle distribution function f_i with a general forcing term $\boldsymbol{F}$ can be written as:

$$\frac{\mathrm{D}f_i}{\mathrm{D}t} = \boldsymbol{\Omega}_f + \frac{f_i^{(\mathrm{eq})}}{\rho c_s^2}(\boldsymbol{c}_i - \boldsymbol{u}) \cdot \boldsymbol{F}, \tag{12}$$

where $\mathrm{D}/\mathrm{D}t := \partial_t + \boldsymbol{c}_i \cdot \nabla$ is the total derivative along the characteristics, $\boldsymbol{\Omega}_f$ is the collision term (to be specified later), and $f_i^{(\mathrm{eq})} = \rho \Gamma_i$ in which Γ_i is defined in Eq. (6). Since the hydrodynamic pressure p is the primary quantity of interest, we make the following change of variable

$$g_i = c_s^2 f_i + w_i(p - p_0), \tag{13}$$

where $p_0 = \rho c_s^2$ is the ideal gas equation of state. The evolution equation for g_i then reads as

$$\frac{\mathrm{D}g_i}{\mathrm{D}t} = \boldsymbol{\Omega}_g + \Gamma_i(\boldsymbol{c}_i - \boldsymbol{u}) \cdot \boldsymbol{F} + w_i \frac{\mathrm{D}(p - p_0)}{\mathrm{D}t}, \tag{14}$$

where $\boldsymbol{\Omega}_g = c_s^2 \boldsymbol{\Omega}_f$ (see Eq. (26)). Both p and p_0 are conserved quantities, that is for incompressible flows $\partial_t p + \boldsymbol{u} \cdot \nabla p = 0$ and $\partial_t p_0 + \boldsymbol{u} \cdot \nabla p_0 = 0$. Thus

$$w_i \frac{\mathrm{D}(p - p_0)}{\mathrm{D}t} = w_i(\boldsymbol{c}_i - \boldsymbol{u}) \cdot \nabla(p - p_0). \tag{15}$$

The forcing term $\boldsymbol{F}$ may be written as

$$\boldsymbol{F} = -\nabla(p - p_0) + \boldsymbol{F}_s + \boldsymbol{F}_b, \tag{16}$$

where the term $(p - p_0)$ accounts for deviations from ideal gas in the equation of state, $\boldsymbol{F}_\mathrm{b}$ is the body force, and $\boldsymbol{F}_\mathrm{s}$ is the interfacial tension force (see Eq. (31)). Substituting Eqs. (15) and (16) in Eq. (14) and neglecting the term $(\Gamma_i - w_i)\nabla p \sim O(\mathrm{Ma}^3)$ leads to

$$\frac{\mathrm{D}g_i}{\mathrm{D}t} = \boldsymbol{\Omega}_g + G_i, \tag{17}$$

where

$$G_i = (\boldsymbol{c}_i - \boldsymbol{u}) \cdot [(\Gamma_i - w_i)\nabla p_0 + \Gamma_i(\boldsymbol{F}_\mathrm{s} + \boldsymbol{F}_\mathrm{b})]. \tag{18}$$

Because the right-hand side of Eq. (17) is a function of g_i, the discretized version of Eq. (17) is implicit. However, it can be made explicit by a simple change of variable:

$$\bar{g}_i = g_i - \frac{\delta t}{2}\left(\boldsymbol{\Omega}_g + G_i\right). \tag{19}$$

This is equivalent to using the following modified equilibrium for g_i

$$\bar{g}_i^{(\mathrm{eq})} = g_i^{(\mathrm{eq})} - \frac{\delta t}{2} G_i. \tag{20}$$

The conserved quantities are now $\rho \boldsymbol{u}$ and p:

$$\rho \boldsymbol{u} = \frac{1}{c_s^2} \sum_i \bar{g}_i \boldsymbol{c}_i + \frac{\delta t}{2}(\boldsymbol{F}_\mathrm{s} + \boldsymbol{F}_\mathrm{b}), \tag{21}$$

$$p = \sum_i \bar{g}_i + \frac{\delta t}{2} \boldsymbol{u} \cdot \nabla p_0. \tag{22}$$

It is worth noting that the updated velocity is used to calculate the pressure in Eq. (22).

Equation (17) can be treated with Strang splitting [45], and the resulting algorithm consists of two steps:

$$\text{collision:} \qquad \bar{g}_i^*(\boldsymbol{x}, t) = \bar{g}_i(\boldsymbol{x}, t) + \boldsymbol{\Omega}_g + G_i, \tag{23a}$$

$$\text{advection:} \qquad \frac{\partial \bar{g}_i^*}{\partial t} + \boldsymbol{c}_i \cdot \nabla \bar{g}_i^* = 0, \tag{23b}$$

where the asterisk denotes the post-collision state and all terms on the right-hand side of Eq. (23a) are evaluated at $(\boldsymbol{x}, t)$. Again, on uniform grids ($\delta x = \delta t$) perfect shift or *streaming* is the solution to the advection equation

$$\bar{g}_i(\boldsymbol{x}, t+\delta t) = \bar{g}_i^*(\boldsymbol{x} - \boldsymbol{c}_i \delta t, t). \tag{24}$$

The following Navier–Stokes equation for incompressible multiphase flows is recovered from the above LB equations

$$\rho\left(\partial_t \boldsymbol{u} + \boldsymbol{u}\cdot\nabla\boldsymbol{u}\right) = -\nabla p + \nabla\cdot\sigma + \boldsymbol{F}_\mathrm{s} + \boldsymbol{F}_\mathrm{b}, \quad \sigma := \mu\left[\nabla\boldsymbol{u} + (\nabla\boldsymbol{u})^T\right]. \tag{25}$$

4. Numerical implementation

4.1. Collision operators

In this study we use the weighted multiple-relaxation-time (WMRT) collision [14] (see Appendix A)

$$\boldsymbol{\Omega}_g = -\mathbf{M}^{-1}\cdot\mathbf{S}\cdot(\mathbf{m} - \mathbf{m}^{(\mathrm{eq})}), \tag{26}$$

where $\mathbf{M}^{-1}$ is the inverse of the orthogonal transformation matrix $\mathbf{M}$, which transforms the distribution functions from physical space to moment space, $\mathbf{S}$ is the diagonal relaxation matrix, and $\mathbf{m} = \mathbf{M}\cdot\bar{\mathbf{g}}$ and $\mathbf{m}^{(\mathrm{eq})} = \mathbf{M}\cdot\bar{\mathbf{g}}^{(\mathrm{eq})}$ are the moments of the distribution function (see Appendix A).

The focus of this work is not the optimization of relaxation rates for accuracy and stability. Therefore, only the relaxation rates of the second-order moments, which are related to shear stresses, vary according to the kinematic viscosity of the fluid (see Eq. (29)), and all other relaxation rates are simply set to one. In other words, the conserved quantities and non-hydrodynamic modes are relaxed to their equilibrium values. This means that for the common 3D lattices

$$\mathbf{S} = \mathrm{diag}(\underbrace{1,\ 1,\ 1,\ 1}_{(d+1)},\ \underbrace{s_\nu,\ s_\nu,\ s_\nu,\ s_\nu,\ s_\nu}_{(d+2)(d-1)/2},\ \underbrace{1,\ 1,\ \ldots,\ 1}_{q-d(d+3)/2}) \tag{27}$$

and

$$s_\nu = \frac{1}{\tau + 1/2}, \tag{28}$$

where τ is the relaxation time, which is related to the kinematic viscosity by

$$\nu = \tau c_s^2 \delta t. \tag{29}$$

If we set all the relaxation rates in Eq. (27) equal to s_ν, then the commonly used BGK or SRT model is recovered, with $\boldsymbol{\Omega}_g = -\frac{\bar{g}_i - \bar{g}_i^{(\mathrm{eq})}}{\tau + 1/2}$. It is well-known that the BGK model causes numerical instabilities as the relaxation time approaches 0. In order to achieve small relaxation times, which correspond to high Reynolds numbers, employing the MRT collision model is inevitable. We must emphasize that the classical MRT model for the D3Q27 lattice [46,47] becomes unstable using the relaxation rates in Eq. (27) [15]. The proposed D3Q27 WMRT model, however, gives us stable and accurate solutions as will be shown.

The materials presented so far are adequate for writing a computer program for numerical simulation of two-phase flows on uniform grids. On the down side, however, it might be very costly to carry out 3D computations with sufficient grid resolution. Although the proposed LB model has the advantage of being highly scalable on massively parallel machines, computational resources (hardware storage and time) can still be a bottle-neck for efficient study of multiscale phenomena. To rectify this issue, we will formulate the model on structured, nonuniform grids in the following section, and incorporate it into an AMR framework (see Sec. 4.4). As will be seen in Sec. 5, the AMR algorithm plays a key role in achieving high efficiency in saving computational resources while producing reasonably accurate results. The major obstacle, particularly for new users who are not familiar with AMR, is that writing an AMR algorithm can be challenging, cumbersome, and time-consuming.

4.2. Nonuniform grids

One way to utilize LBM on nonuniform grids, where the grid spacing Δx is an integer multiple of the finest grid spacing δx, is to discretize the advection equation using a finite-difference scheme [27]. The upwind Euler scheme would be too dissipative and reduces the accuracy of LBM to first order. To retain second-order accuracy of the LBM on nonuniform grids, we solve the advection equation using the following Lax–Wendroff scheme [48,26]:

$$\begin{aligned} f_i(\boldsymbol{x}, t+\delta t) = {} & f_i^*(\boldsymbol{x}, t) - C\left[f_i^*(\boldsymbol{x}, t) - f_i^*(\boldsymbol{x} - \boldsymbol{e}_i\Delta x, t)\right] \\ & - \frac{1}{2}C(1-C)\left[f_i^*(\boldsymbol{x} + \boldsymbol{e}_i\Delta x, t) - 2f_i^*(\boldsymbol{x}, t) + f_i^*(\boldsymbol{x} - \boldsymbol{e}_i\Delta x, t)\right], \end{aligned} \tag{30}$$

where f_i here is a placeholder for either of the distribution functions (h_i or $\bar{g}_i$), $\boldsymbol{e}_i = \boldsymbol{c}_i/c$ is the dimensionless velocity set, and $C := c\delta t/\Delta x = \delta x/\Delta x$ is the Courant–Friedrichs–Lewy (CFL) number. As can be seen in the above equation, when $C = 1$ the Lax–Wendroff equation becomes the perfect shift, which is the exact solution to the advection equation. This is the case when the spatial grid resolution is such that $\Delta x = \delta x$, and is favorable because the perfect shift solution eliminates any numerical error due to dispersion or dissipation, which stem from the finite-difference approximation of the advection equation. This feature is fully exploited by using the AMR algorithm described in Sec. 4.4.

4.3. Calculation of the gradients

The surface tension force can be calculated by

$$\boldsymbol{F}_s = \mu_\phi \nabla\phi, \tag{31}$$

where

$$\mu_\phi = 4\beta\phi\,(\phi-1)\left(\phi-\frac{1}{2}\right) - \kappa\nabla^2\phi \tag{32}$$

is the chemical potential. Coefficients β and κ are related to the surface tension σ and interface width ξ by $\beta = 12\sigma/\xi$ and $\kappa = 3\sigma\xi/2$. With the exception of the distribution functions needed to complete the advection step, as in any single-phase LB model, the only non-local variable here is the phase field. Compared to other existing LB models for multiphase flows this is advantageous because the efficiency of the numerical scheme is increased by enhancing the locality of the LBE, making the model more practical for parallel implementation.

All the derivatives are calculated using second-order finite-differences. The gradient of the phase-field variable, which appears in the computation of the normal to the interface in Eq. (2) and in the computation of macroscopic properties in Eqs. (21) and (22), is calculated using the following second-order isotropic differences

$$\nabla\phi = \frac{3}{\Delta x}\sum_i \boldsymbol{e}_i w_i \phi(\boldsymbol{x}+\boldsymbol{e}_i\Delta x, t). \tag{33}$$

To avoid division by zero in calculation of Eq. (2), a small number (10^{-12}) is added in the computation of the magnitude of the phase-field gradient in the denominator. The Laplacian term in Eq. (32) is calculated using the following isotropic differences with second-order accuracy

$$\nabla^2\phi = \frac{6}{(\Delta x)^2}\sum_i w_i\left[\phi(\boldsymbol{x}+\boldsymbol{e}_i\Delta x, t) - \phi(\boldsymbol{x}, t)\right]. \tag{34}$$

On the other hand, Eq. (18) includes first derivatives of the phase-field ($\nabla p_0 = c_s^2\nabla\rho = c_s^2(\rho_H - \rho_L)\nabla\phi$ and $\boldsymbol{F}_s = \mu_\phi\nabla\phi$) which are multiplied by the microscopic velocity set ($\boldsymbol{c}_i\cdot\nabla$). These terms are treated as directional derivatives along characteristics [49]. For calculation of the modified equilibrium distribution function in Eq. (20), the directional derivatives that appear in G_i in Eq. (18) are discretized using

$$\boldsymbol{e}_i\cdot\nabla\phi|_{(\boldsymbol{x},t)} = \frac{1}{2\Delta x}\left[\phi(\boldsymbol{x}+\boldsymbol{e}_i\Delta x, t) - \phi(\boldsymbol{x}-\boldsymbol{e}_i\Delta x, t)\right], \tag{35}$$

and the directional derivatives that appear in calculation of G_i in the collision step in Eq. (23a) are discretized using

$$\boldsymbol{e}_i\cdot\nabla\phi|_{(\boldsymbol{x},t)} = \frac{-1}{4\Delta x}\left[\phi(\boldsymbol{x}+2\boldsymbol{e}_i\Delta x, t) - 5\phi(\boldsymbol{x}+\boldsymbol{e}_i\Delta x, t) + 3\phi(\boldsymbol{x}, t) + \phi(\boldsymbol{x}-\boldsymbol{e}_i\Delta x, t)\right]. \tag{36}$$

It is worth noting that using mixed differences has been shown to compromise momentum conservation [50]. Although we can employ isotropic differences to calculate all the gradients [51], in this study we use mixed differences only in calculation of the collision step in Eq. (23a).

4.4. Adaptive mesh refinement in 3D

Roughly speaking, two orders of magnitude reduction in computer hardware storage and speed-up in the computations are achieved by implementing the proposed 3D AMR algorithm. In addition, post-processing of the output data is much more efficient due to significant reduction in the size of the output files. The 3D AMR algorithm implemented in this paper is a direct extension of the cell-centered AMR structure previously proposed in 2D [27,28]. Here, we briefly introduce the necessary parameters and nomenclature, and refer the interested reader to Refs. [26,27] for full details of the algorithm.

The AMR hierarchy is built by using structured, cubic blocks. All blocks are self-similar in the sense that they consist of $n_x \times n_y \times n_z$ cells with different grid spacings characterized by their refinement level l. The base block is the coarsest one with $l = 0$, and the grid spacing for each block is

$$\Delta x = \frac{L_x}{n_x 2^l} = \frac{L_y}{n_y 2^l} = \frac{L_z}{n_z 2^l}, \tag{37}$$

where L_x, L_y, and L_z are the size of the base block in the x-, y-, and z-directions, respectively. In the current work we use $n_x = n_y = n_z = 8$.

Once the computational domain is covered with a sufficient number of base blocks, the so-called refinement criteria (see Sec. 4.4.1) are used to identify zones where higher resolution is needed, e.g., in the vicinity of the interface between different fluids. Accordingly, those blocks in the desired regions are flagged for refinement. The actual refinement/coarsening automation is triggered by noting that the difference in the refinement level between two adjacent blocks cannot exceed one. This process is repeated until the number of refinement levels reaches a maximum input value. The value of this maximum allowable refinement level is assigned by taking into account the limit of available computational resources, i.e., time and memory. This also ensures that the blocks are not generated indefinitely.

Once the AMR hierarchy is built, we need a means for communicating the nonlocal variables, i.e., h_i^*, $\bar{g}_i^*$, and ϕ for our purposes, between adjacent blocks. This is achieved by using pointers to determine the neighboring blocks and by using ghost cells to communicate the necessary data. In 2D the data is communicated with eight neighboring blocks, while in 3D inter-block communications go up to 26 neighbors. When two neighboring blocks are at the same refinement level the ghost cells are directly filled by a simple copy. Otherwise, triquadratic interpolations, essential to a spatially second-order accurate solution [52,26,27], are used to obtain the unknown distribution functions (h_i^* and $\bar{g}_i^*$) and phase field (ϕ). It is worth mentioning that only one layer of data, in each direction, is assigned as ghost cells for the distribution functions while two layers are assigned for the phase-field variable due to the use of second-order biased differences (see Eq. (36)). For boundary blocks, a negative pointer value is assigned to specify the type of boundary condition to be applied.

Once again, it is worth noting that Δx and δt in our model are not the same because we solve the advection equation using the Lax–Wendroff scheme, which decouples space and time. Therefore, all the blocks are advanced in time simultaneously using the same time step but different grid spacing. We do, however, use $\Delta x = \delta x = 1$ ($C = 1$) on the blocks at the finest refinement level (finest grids) to obtain the most accurate results (as mentioned in Sec. 4.2, the perfect shift is the solution of the advection equation on these finest blocks). This also eliminates any dispersion error pertinent to the Lax–Wendroff scheme in the vicinity of interfacial regions, where higher accuracy is desirable. Therefore, an interesting feature of the LBM, that is the perfect shift or streaming, is properly utilized on nonuniform grids.

4.4.1. Refinement criteria

For automation of the AMR, a reliable refinement criterion, or a so-called feature-detecting estimator, is required. Once the refinement criterion within a certain block is above a threshold value ϵ_r it is flagged for refinement. Likewise, if the refinement criterion in all leaf blocks of a given parent block is below a prescribed value ϵ_d the parent block is flagged for coarsening or derefinement. For multiphase flows we use the following refinement criterion ϵ

$$\epsilon = |\nabla \phi| = \sqrt{\left(\frac{\partial \phi}{\partial x}\right)^2 + \left(\frac{\partial \phi}{\partial y}\right)^2 + \left(\frac{\partial \phi}{\partial z}\right)^2}, \tag{38}$$

which is sensitive to noticeable changes in the phase field, and so a good measure for resolving interfacial regions. We have found the following values $\epsilon_r = 0.002$ and $\epsilon_d = 0.001$ to yield reasonably accurate and efficient simulations [28].

5. Numerical validations

Here we present several simulations, representative of multiphase flow problems of practical and scientific interest, to assess the proposed WMRT–LBM–AMR in 3D. In what follows, we use the characteristic domain size $L_0 = N\delta x$, where N is the equivalent number of grid points on a uniform grid, which might be different than grid spacing ($\delta x \leq \Delta x$), to nondimensionalize the length. We present the results in terms of the density ratio $\rho^* = \rho_H/\rho_L$ and viscosity ratio $\mu^* = \mu_H/\mu_L$, where μ_H and μ_L are the viscosities of the heavy and light fluids, respectively. The simulations are executed using the Intel compiler in release mode (O3 optimization) on a personal computer with an Intel® Core™ i7-4910MQ processor (CPU) @2.90 GHz base frequency and 32 GB shared memory (RAM).

5.1. Mass conservation

To begin, we demonstrate the ability of the proposed WMRT–LBM, without AMR, to conserve mass by comparing a Cahn–Hilliard-based LBM [49] and the current conservative phase-field model [28]. To this end, we place a circular droplet with dimensionless radius $R^* = R/L_0 = 0.25$ in the middle of a periodic domain. The liquid droplet is surrounded by a stationary gas phase ($\rho^* = 1000$ and $\mu^* = 100$). The shape of the droplet at initial time and after 20000 iterations is shown in Fig. 1 for two different LB models. As can be seen, the droplet in the Cahn–Hilliard-based model loses its mass and shrinks with time, while the mass of the droplet using the current model remains constant (to within round-off error). This is why we call the current LB model “mass conserving”. However, when combined with the AMR technique in Sec. 4.4, the proposed model does not exactly conserve mass due to interpolation at the borders of different blocks and due to dispersion

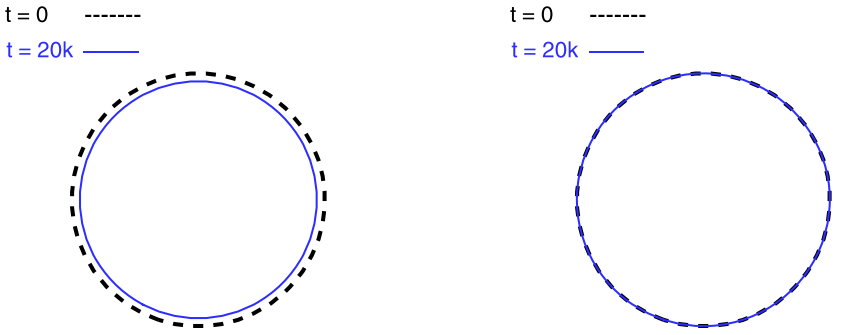

(a) Cahn-Hilliard LBM (b) Conservative LBM

Fig. 1. Stationary droplet test with $\rho^* = 1000$ and $\mu^* = 100$. (a) Cahn–Hilliard-based LBM [49]; (b) Current phase-field LBM [28].

errors associated with the Lax–Wendroff method. Nevertheless, any mass conservation issues of the combined AMR–LBM are not as severe as those that arise with Cahn–Hilliard-based models, especially because we use higher resolution in the vicinity of interfaces.

5.2. Rising bubble

The buoyancy-driven motion of a gas bubble in a viscous liquid is an important phenomenon with many scientific and engineering applications [31,32]. Numerical simulation of bubble dynamics is more challenging than droplet dynamics because the (inertial and viscous) forces exerted on the gas bubble are stronger. We have previously studied a similar problem at $\rho^* = 10$ in axisymmetric coordinates [53]. In this paper we consider a fully 3D bubble rising in a viscous liquid, typical of an air–water system, to assess the proposed model in terms of accuracy and efficiency.

The computational domain depicted in Fig. 2 is a right rectangular prism of size $(1, 4, 1)$, which is equivalent to a uniform grid of resolution $256 \times 1024 \times 256$. Initially, we place a spherical gas bubble with $R^* = 0.125$ at $(0, 1, 0)$. We take advantage of the symmetry of the problem with respect to the x and z axes and use symmetric boundary conditions at $x = 0$ and $z = 0$. The volumetric buoyancy force $\boldsymbol{F}_b = (\rho_{\rm H} - \rho) g_y \hat{\boldsymbol{y}}$, where g_y is the magnitude of gravitational acceleration, is applied in the vertical direction $\hat{\boldsymbol{y}}$, with bounce-back boundary conditions at the bottom ($y = 1$), top ($y = 4$), right ($x = 1$), and front ($z = 1$) boundaries. In this section, the computations are performed using the D3Q27 lattice.

In addition to the density and viscosity ratios, the flow can be characterized by the gravity Reynolds number

$$\mathrm{Re}_{\rm Gr} = \frac{\rho_{\rm H} \sqrt{g_y D^3}}{\mu_{\rm H}}, \tag{39}$$

where D is the drop diameter, and the Eötvös number

$$\mathrm{Eo} = \frac{g_y \rho_{\rm H} D^2}{\sigma}. \tag{40}$$

In the literature, the Eötvös number is usually accompanied by the Morton number

$$\mathrm{Mo} = \frac{g_y \mu_{\rm H}^4}{\rho_{\rm H} \sigma^3}. \tag{41}$$

The dimensionless time is also defined by

$$t^* = t \sqrt{\frac{g_y}{D}}. \tag{42}$$

A variety of shapes that the bubble attains with $\rho^* = 1000$, $\mu^* = 100$, and different values of the pertinent dimensionless numbers at $t^* = 10$, when it has roughly reached its terminal rise velocity u_t, are shown in Fig. 3. In this section, the numerical values for the interface thickness and mobility are $\xi = 5$ lu and $M = 0.04$ lu, respectively. Our results are qualitatively similar to experimental observations by Bhaga and Weber [32]. Spherical and ellipsoidal bubbles are observed at low to intermediate Eötvös numbers, while at higher Eötvös numbers spherical-cap and skirted bubbles are formed. These are also consistent with the bubble map in Ref. [31].

Additionally, we calculate and compare the drag coefficient of the bubble versus experimental data given by [32]:

$$C_D^{\rm exp} = \left[2.67^{0.9} + \left(\frac{16}{\mathrm{Re}} \right)^{0.9} \right]^{\frac{1}{0.9}}, \tag{43}$$

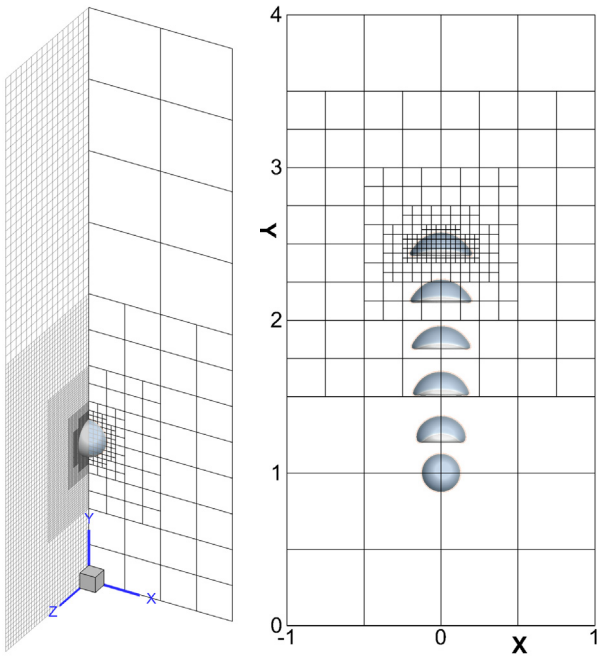

(a) (b)

Fig. 2. Rising bubble setup. (a) Initial configuration showing the edge of AMR block (on the x–y plane) and the grid resolution (on the y–z plane); (b) plane view of the evolution of the bubble with $\rho^* = 1000$, $\mu^* = 100$, $\mathrm{Re_{Gr}} = 40$, and $\mathrm{Eo} = 40$ ($\mathrm{Mo} = 2.50 \times 10^{-2}$). The flood contours show the phase field at $t^* = 0$–10 with $\Delta t^* = 2$.

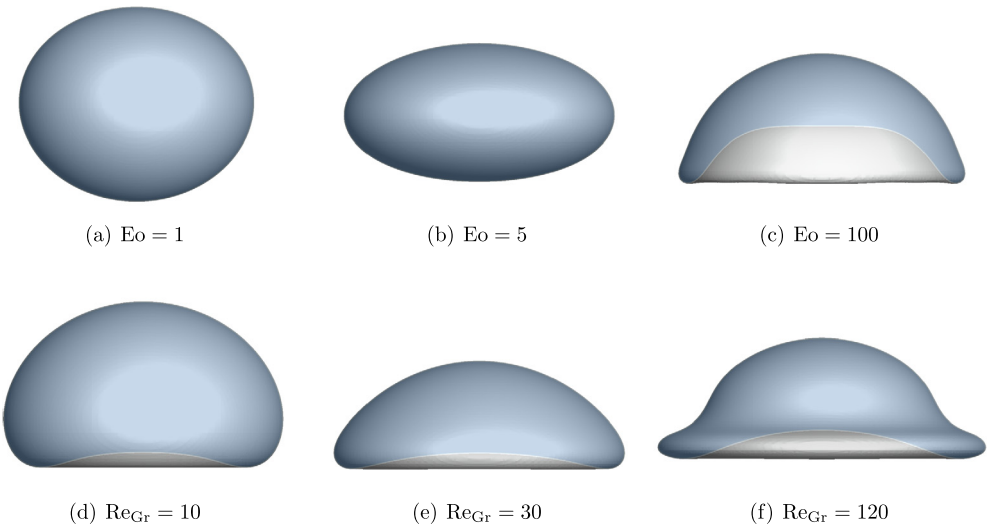

(a) $\mathrm{Eo} = 1$ (b) $\mathrm{Eo} = 5$ (c) $\mathrm{Eo} = 100$

(d) $\mathrm{Re_{Gr}} = 10$ (e) $\mathrm{Re_{Gr}} = 30$ (f) $\mathrm{Re_{Gr}} = 120$

Fig. 3. Terminal shape of the rising bubble with $\rho^* = 1000$ and $\mu^* = 100$ under different conditions at $t^* = 10$. The top row is at a constant gravity Reynolds number ($\mathrm{Re_{Gr}} = 40$) and the bottom row is at a constant Eötvös number ($\mathrm{Eo} = 30$). (a) $\mathrm{Re_{Gr}} = 40$, $\mathrm{Eo} = 1$ ($\mathrm{Mo} = 3.91 \times 10^{-7}$); (b) $\mathrm{Re_{Gr}} = 40$, $\mathrm{Eo} = 5$ ($\mathrm{Mo} = 4.88 \times 10^{-5}$); (c) $\mathrm{Re_{Gr}} = 40$, $\mathrm{Eo} = 100$ ($\mathrm{Mo} = 3.91 \times 10^{-1}$); (d) $\mathrm{Re_{Gr}} = 10$, $\mathrm{Eo} = 30$ ($\mathrm{Mo} = 2.70$); (e) $\mathrm{Re_{Gr}} = 30$, $\mathrm{Eo} = 30$ ($\mathrm{Mo} = 3.33 \times 10^{-2}$); (f) $\mathrm{Re_{Gr}} = 120$, $\mathrm{Eo} = 30$ ($\mathrm{Mo} = 1.30 \times 10^{-4}$).

where $\mathrm{Re} = \rho_\mathrm{H} u_t D / \mu_\mathrm{H}$. The numerical drag coefficient can be obtained by balancing the buoyancy and inertial forces, which for a spherical bubble becomes

$$C_D^{\mathrm{LBM}} = \frac{4}{3} \frac{g_y (\rho_\mathrm{H} - \rho_\mathrm{L}) D}{\rho_\mathrm{H} u_t^2}. \tag{44}$$

The numerical findings, together with experimental data from Eq. (43), are plotted against the Reynolds number in Fig. 4. As can be seen, the numerical results are in good agreement with experimental data. It is worth noting that each simulation,

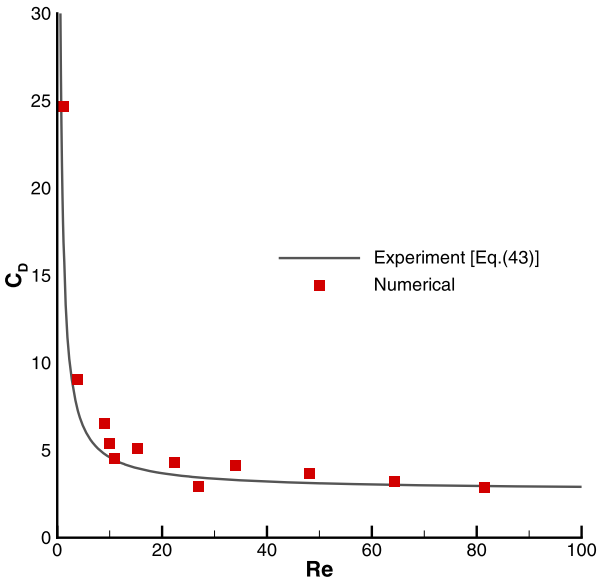

Fig. 4. Drag coefficient for a rising bubble ($\rho^* = 1000$ and $\mu^* = 100$). Comparison between experimental data shown by the solid black line [32] and current AMR–LBM shown by red square symbols. (For interpretation of the references to color in this figure legend, the reader is referred to the web version of this article.)

which takes about 4 h to run on a laptop with four processors, is performed about 200 times faster than a simulation on an equivalent uniform grid. Moreover, the savings in hardware and memory resources are roughly two orders of magnitude, with an additional saving in computational cost (both hardware and time) for post processing of the output data files, which are about 80 times smaller than those obtained from a uniform grid.

5.3. Breakup of a falling drop

The deformation and breakup of a falling droplet under buoyancy is an interesting phenomenon which has been studied numerically by many authors [54–56]. A liquid droplet of dimensionless radius $R^* = 0.125$ is placed at $(0, 3.5, 0)$ within a computational domain of size $(1, 4, 1)$ with symmetric boundaries at $x = 0$ and $z = 0$ as shown in Fig. 5(a). No-slip, link bounce-back boundary conditions are applied at the bottom and top faces of the domain with Neumann boundary conditions at $x = 1$ and $z = 1$. The buoyancy force $\boldsymbol{F}_b = (\rho_L - \rho) g_y \hat{\boldsymbol{y}}$ is applied to the entire fluid. In addition to ρ^* and μ^*, the flow is characterized by two principle dimensionless numbers: the Bond number

$$\mathrm{Bo} = \frac{g_y(\rho_H - \rho_L)D^2}{\sigma} \tag{45}$$

and the Ohnesorge number

$$\mathrm{Oh} = \frac{\mu_H}{\sqrt{\rho_H \sigma D}}. \tag{46}$$

Here we consider deformation of the falling drop with $\rho^* = 10$, $\mu^* = 2$, $\mathrm{Bo} = 200$, and $\mathrm{Oh} = 0.15$ using the D3Q19 lattice with $\xi = 4$ lu and $M = 0.015$ lu. The Bond number, which quantifies the relative importance of buoyancy to surface tension forces, is chosen large enough to ensure a rather drastic deformation in the topology of the falling drop. These parameters are chosen in such a way as to observe the well-known *bag-breakup* mode of the falling drop [54,57].

The mid-plane ($z = 0$) view of the evolution of the drop as it falls is plotted in Fig. 5(b). The formation of a bag-shaped drop is evident at $t^* = 4.2$. As time goes on, pressure forces prevail over interfacial tensions and the bag becomes thinner. Eventually, the thin bag breaks into multiple droplets at $t^* = 5.4$. Fig. 6 shows the streamlines around the falling drop at an intermediate time and moments before initiation of the bag breakup. The mechanism of creation and breakup of the bag-shaped drop is also illustrated in 3D in Fig. 7 at different times. The simulation of the bag breakup mechanism is in good agreement with experimental observations [33]. As can be seen in Fig. 7, the flow field is no longer axisymmetric at late times, which highlights the fully 3D nature of this breakup mechanism. Axisymmetric simulations [54,57] are indeed inadequate for capturing such details [56].

5.4. Drop splashing on a wet surface

The dynamics of a drop impacting an already wet surface is another computationally demanding phenomenon of broad interest. In addition to challenges associated with large density and viscosity contrasts, this problem has the extra difficulty

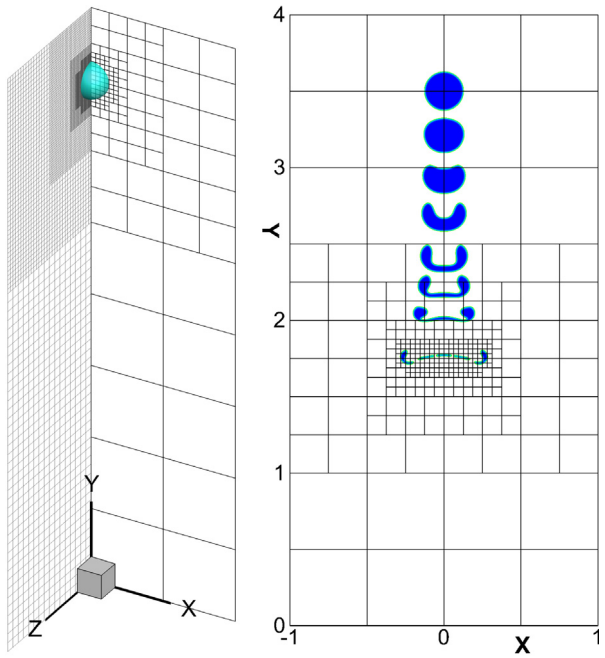

(a) (b)

Fig. 5. Falling droplet ($\rho^* = 10$, $\mu^* = 2$, Bo = 200, Oh = 0.15). (a) Initial configuration at $t^* = 0$; (b) 2D view of the evolution of the falling drop. The flood contours show the phase field at $t^* = 0$, 1.8, 2.6, 3.2, 3.8, 4.2, 4.6, and 5.4, sequentially.

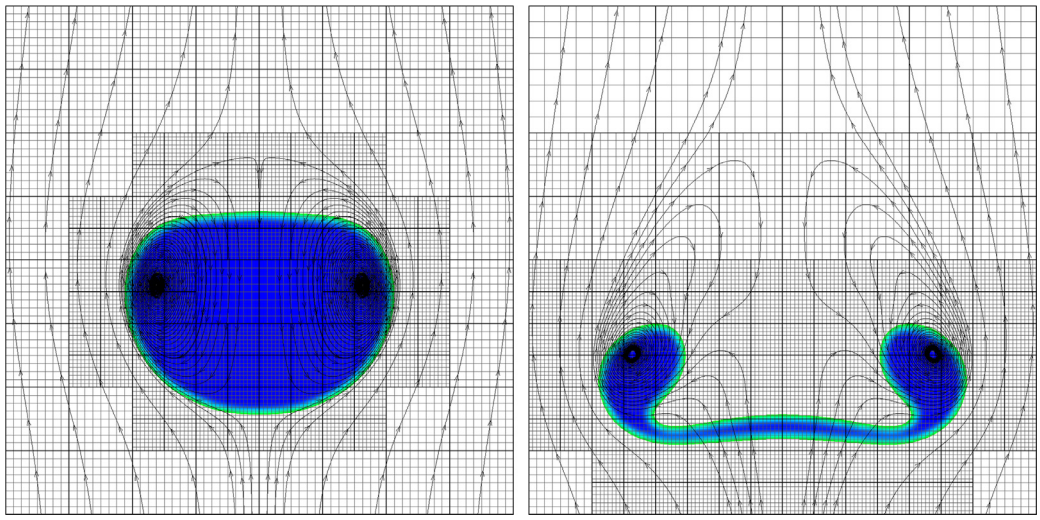

(a) $t^* = 2.2$ (b) $t^* = 4.4$

Fig. 6. 2D view of the streamlines around the falling droplet ($\rho^* = 10$, $\mu^* = 2$, Bo = 200, Oh = 0.15).

of a singularity at the impact point. We choose this specific problem to asses the accuracy and feasibility of the proposed model to simulate such flows with rapid topological changes. In addition to the density and viscosity ratios, two additional dimensionless numbers naturally arise: the Reynolds number

$$\mathrm{Re} = \frac{\rho_{\mathrm{H}} U_0 D}{\mu_{\mathrm{H}}} \tag{47}$$

and the Weber number

$$\mathrm{We} = \frac{\rho_{\mathrm{H}} U_0^2 D}{\sigma}, \tag{48}$$

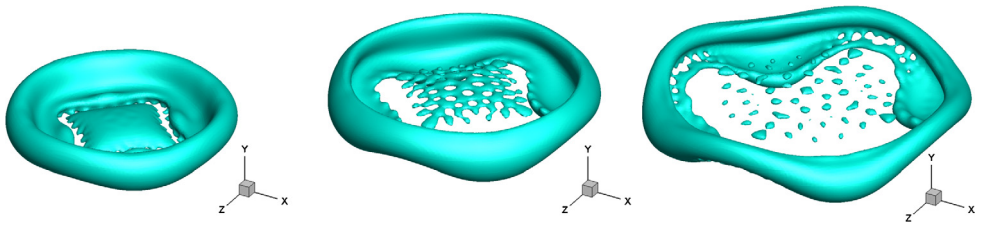

(a) $t^* = 5.0$ (b) $t^* = 5.4$ (c) $t^* = 5.8$

Fig. 7. Bag breakup of the falling droplet ($\rho^* = 10$, $\mu^* = 2$, Bo = 200, Oh = 0.15).

where U_0 is the initial velocity of the drop. For this problem the dimensionless time is defined as $t^* = t\,U_0/D$. Theoretical predictions [34] suggest that the spreading radius r can be estimated as $r = \sqrt{DU_0 t}$, or in dimensionless form

$$r^* = \sqrt{t^*}, \tag{49}$$

where $r^* = r/D$. In Ref. [34], the spreading radius was calculated as the radius of the point where the velocity of the fluid was maximum at a given time. Geometrically, this point was shown to approximately coincide with the contact line between the liquid drop and the wet layer. Using numerical simulations, Josserand and Zaleski [34] found that the spread radius actually follows $r^* = 1.1\sqrt{t^*}$.

Following Josserand and Zaleski [34], we conduct simulations that fall in the range of intermediate to high Reynolds numbers where splashing occurs. We consider two cases with $\rho^* = 500$ and We = 8000 at two different Reynolds numbers. In the first case, Re = 100 and $\mu^* = 400$ while in the second case Re = 1000 and $\mu^* = 40$. The drop is centered at $(1, 0.26, 1)$ in a domain of size $(1, 1, 1)$, which corresponds to a 512^3 grid with symmetric boundaries at $x = 0$ and $z = 0$. The dimensionless radius of the drop is $R^* = 0.2$ and the dimensionless height of the liquid film shown in Fig. 8(a) is 0.06. The boundary conditions are link bounce-back at the bottom and top of the domain and zero-gradient at $x = 1$ and $z = 1$. The simulations are carried out on the D3Q27 lattice with $\xi = 5$ lu and $M = 0.03$ lu.

Fig. 8(a) shows the plane view of the initial configuration, and Figs. 8(b) and 8(c) illustrate the evolution of the edge of the drop over time for Re = 100 and Re = 1000, respectively. As can be seen, the droplet undergoes a smooth, and roughly axisymmetric, splashing at Re = 100. Increasing the Reynolds number to 1000 causes the axisymmetric rim to break into multiple droplets, which is known as crown formation (see Fig. 8(c)).

The 3D snapshot of the impacting drop at $t^* = 2.0$ are shown in Fig. 9 for both Re = 100 and Re = 1000. After the drop impacts the liquid film, a thin liquid sheet (rim) is formed that propagates outwards, radially. Depending on the relative strength of inertial and viscous forces, characterized by the Reynolds number, the rim may become unstable and break up, as is the case for Re = 1000 in Fig. 9(b). The growth rate of the stable rim is expected to follow power-law relation (49). As can be seen in Fig. 10, the spreading radius is in accordance with the theoretical prediction and previous numerical findings ($r^* = 1.1\sqrt{t^*}$ [34]). It is worth highlighting the contrast with 2D results [28], which overestimate the spreading. Also, as can be seen in Fig. 10, the spread radius seems to deviate from the power-law relations at late times. This may be attributed to boundary effects as the droplet gets closer to the edge of the computational domain though the power-law relation is not expected to be accurate at late times [34].

6. Droplet coalescence at a flat interface

A droplet in the vicinity of a flat interface of the same fluid, when undergoing coalescence, exhibits interesting behaviors depending on overriding factors characterized by the interplay of buoyancy, viscous, and interfacial forces [35–41]. In addition to density and viscosity ratios, important dimensionless groups are the Bond and Ohnesorge numbers defined in Eqs. (45) and (46), respectively. For this problem the capillary time, $t_c = \sqrt{\rho_H D^3/\sigma}$, is commonly used to nondimensionalize time such that $t^* = t/t_c$.

The main mechanisms for coalescence of the drop depend on the magnitude of Bo and Oh. Depending on the strength of surface tension, gravity, and viscous forces, a drop may undergo complete coalescence, partial coalescence or rebound, and splashing. Numerical simulation of partial coalescence in particular is complicated by the very small length and time scales that arise from the multiscale nature of this phenomenon.

6.1. Partial coalescence

As our first example, similar to experiments conducted by Chen et al. [38], a liquid drop with $\rho^* \simeq 1.316$ is placed above a flat liquid–liquid interface. The dimensionless groups are identical to those reported in Refs. [38,39]: $\mu^* = 0.5$, $\text{Bo} = 9.59 \times 10^{-2}$, and $\text{Oh} = 5.53 \times 10^{-3}$ (note that in Ref. [38] the Ohnesorge number was defined based on the average density of the fluids).

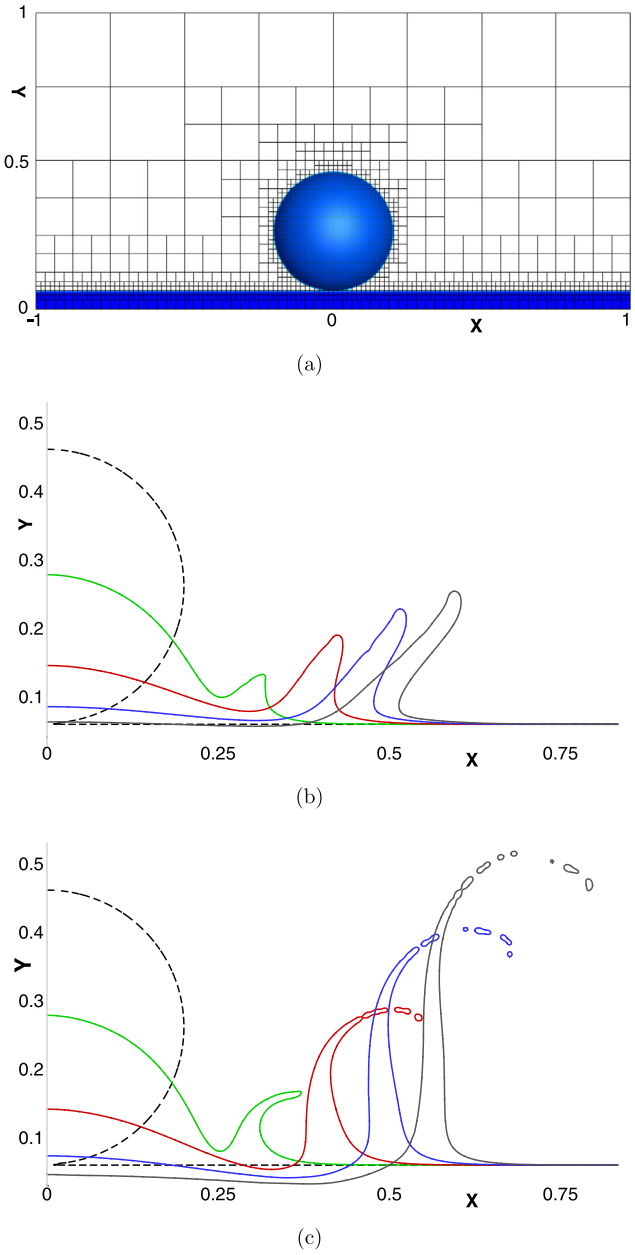

Fig. 8. 2D view of drop impact on a wet surface with $\rho^* = 500$ and $\mathrm{We} = 8000$. The interface profile is shown at (a) initial time ($t^* = 0$), and the evolution of the interface with time is plotted at $t^* = 0$, 0.5, 1.0, 1.5, 2.0 for (b) $\mathrm{Re} = 100$ and $\mu^* = 400$ and (c) $\mathrm{Re} = 1000$ and $\mu^* = 40$.

Initially, a spherical drop of dimensionless radius $R^* = 1/6$ is placed at $(0, 1 + R^* + \delta, 0)$ inside a cubic domain of size $(1, 2, 1)$ where $\delta = 7.8 \times 10^{-3}$ is the dimensionless gap between the lower edge of the drop and the liquid–liquid interface. Symmetric boundary conditions are used at $x = 0$ and $z = 0$ and zero-gradient (Neumann) boundary conditions are imposed at $x = 1$ and $z = 1$. The numerical values of the mobility and interface thickness are $\xi = 3$ lu and $M = 0.015$ lu, respectively (see the discussion in Sec. 6.2). The initial pressure field is approximated to be hydrostatic with a volumetric body force $\boldsymbol{F}_b = -\rho g_y \hat{\boldsymbol{y}}$ applied to the entire fluid. The $z = 0$ view of the computational setup and initial condition is shown in Fig. 11(a). In Fig. 11, the interface is shown by a thick black line and the color contours denote the pressure field, which is normalized by the capillary tension force ($p^* = pD/4\sigma$). Snapshots of the partial coalescence mechanism just before coalescence at $t^* = 0.8$ and moments after pinch-off at $t^* = 1.0$ are shown in Figs. 11(b) and 11(c), respectively.

A side-by-side comparison of the current numerical simulations with the experimental observations in Ref. [38] is shown in Fig. 12. Initially, while the drop is being drained into the liquid pool, a capillary wave (shown by an arrow in the experimental pictures) is generated. The drop then evolves into a cylindrical body of liquid ($t^* = 0.56$) due to the upward

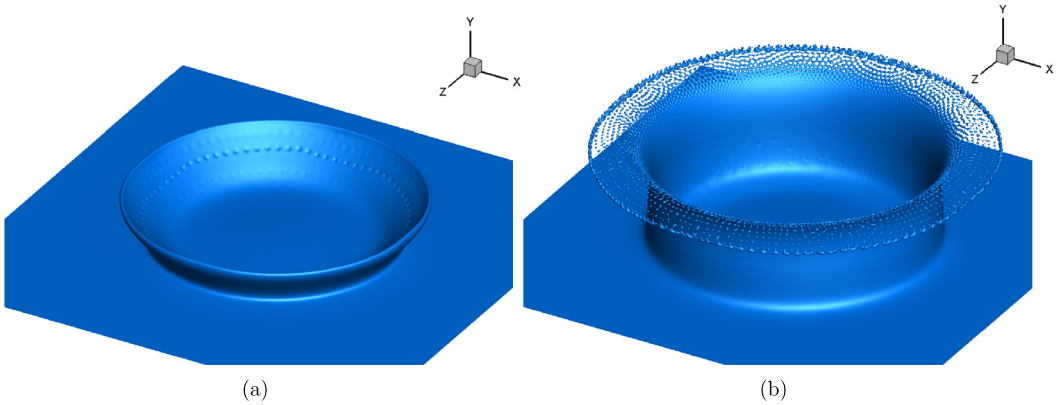

Fig. 9. Drop impact on a wet surface at $t^* = 2.0$ ($\rho^* = 500$, We $= 8000$). (a) Re $= 100$, $\mu^* = 400$; (b) Re $= 1000$, $\mu^* = 40$ (for the video see this link).

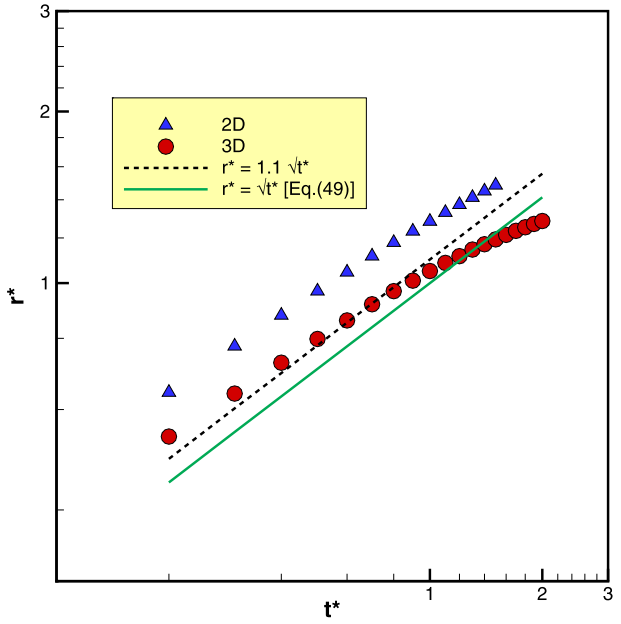

Fig. 10. Theoretical and numerical results of the spreading radius versus time ($\rho^* = 500$, We $= 8000$, Re $= 100$, $\mu^* = 400$).

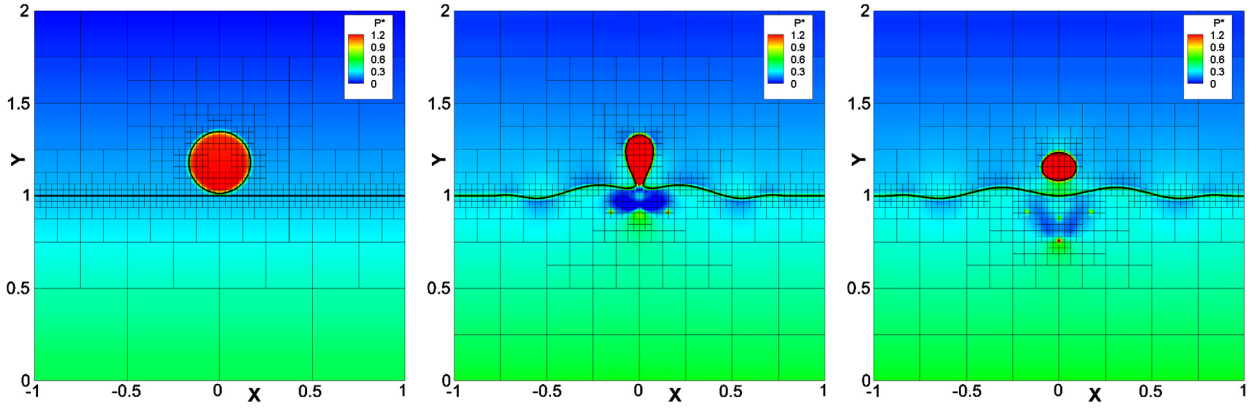

Fig. 11. 2D view of the partial coalescence between a liquid drop and a liquid–liquid interface at different times. $\rho^* = 1.316$, $\mu^* = 0.5$, Bo $= 9.59 \times 10^{-2}$, and Oh $= 5.53 \times 10^{-3}$. The interface is shown by a thick black line and the flood contours show the normalized pressure ($p^* = pD/4\sigma$).

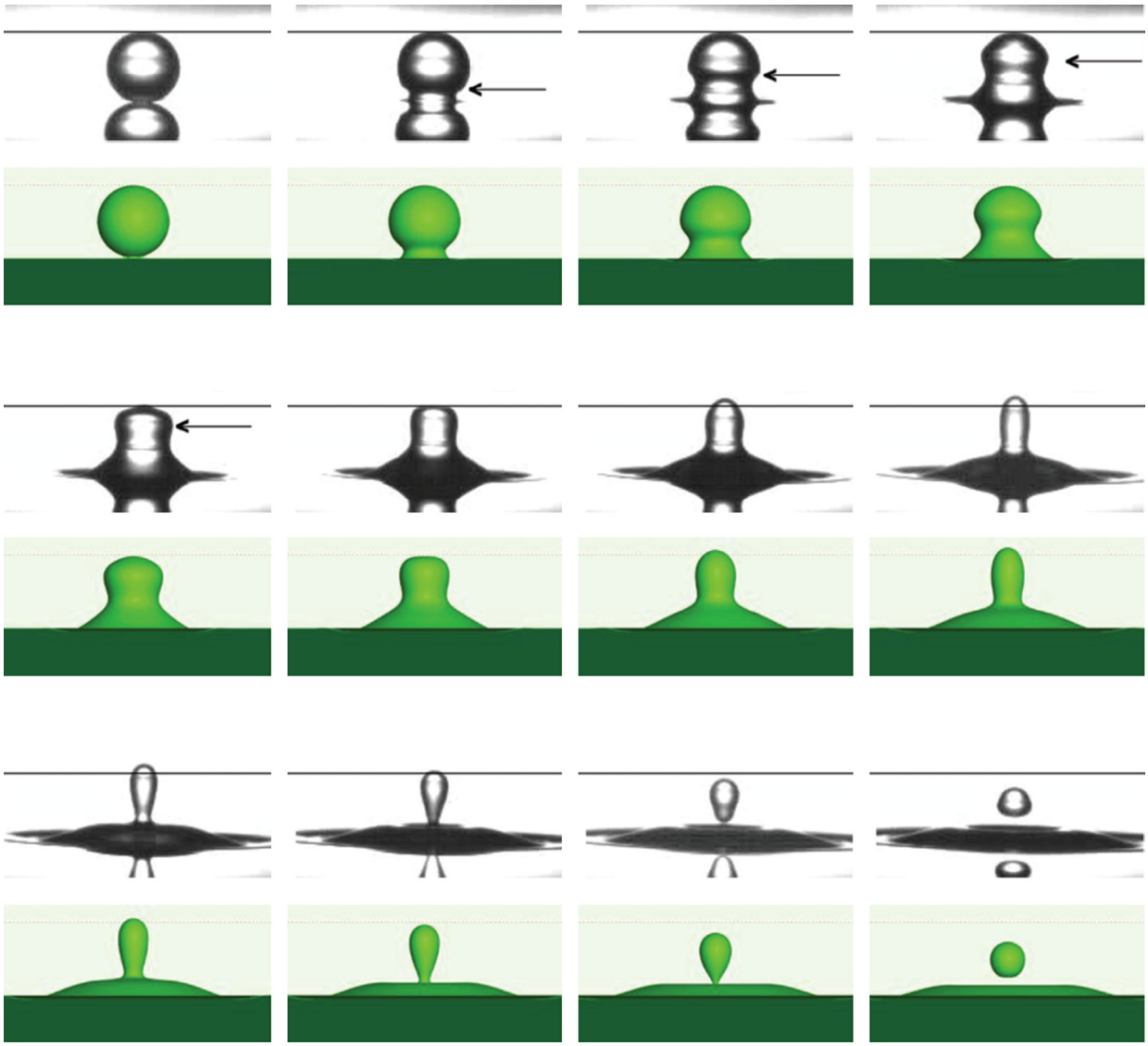

Fig. 12. Partial coalescence between a liquid drop and a liquid–liquid interface. Comparison between the current model and the experiments by Chen et al. [38]. $\rho^* = 1.316$, $\mu^* = 0.5$, $\mathrm{Bo} = 9.59 \times 10^{-2}$, and $\mathrm{Oh} = 5.53 \times 10^{-3}$. The green contour shows the isosurface of $\phi = 0.5$. Solid black lines in experiments and dotted red lines in simulations are the guidelines for tracking the vertical position of the liquid drop. The initial and final times are $t^* = 0$ and $t^* = 0.890$ with $\Delta t^* = 0.081$, which corresponds to 542 microseconds in experiments. (For interpretation of the references to color in this figure legend, the reader is referred to the web version of this article.)

momentum of this capillary wave. Then pinch-off occurs at $t^* = 0.81$, and a daughter droplet can be seen suspended above the deformed liquid pool at $t^* = 0.89$.

6.2. Effect of the mobility

Aside from the physical parameters, the mechanism of drop coalescence onto a fluid interface depends on numerical factors such as the mobility and interface thickness. Although free parameters, these quantities are dictated by numerical stability and accuracy. In order for simulations to approach the sharp-interface solution, it is generally more accurate to use smaller values for the interfacial thickness ξ. However, using a value of ξ that is too small leads to numerical instabilities, especially as the density ratio increases. Similarly, lower values for the mobility are desirable. Having a too large a mobility results in excessive numerical dissipation in the system which in turn leads to inaccurate results [58]. In our simulations we obtain numerically stable and reasonably accurate results by choosing $\xi \sim 3$–5 lu and $M \sim 0.01$–0.05 lu, which correspond to the numerical Péclet number $\mathrm{Pe} = \frac{\sqrt{g_y D^3}}{M}$ of 75–3. Specifically, from experience, we recommend using $\xi = 3$ lu and $M = 0.01$–0.02 lu when $\rho^* = 1$–10, $\xi = 4$ lu and $M = 0.02$–0.03 lu when $\rho^* = 10$–100, and $\xi = 5$ lu and $M = 0.03$–0.05 lu when $\rho^* = 100$–1000.

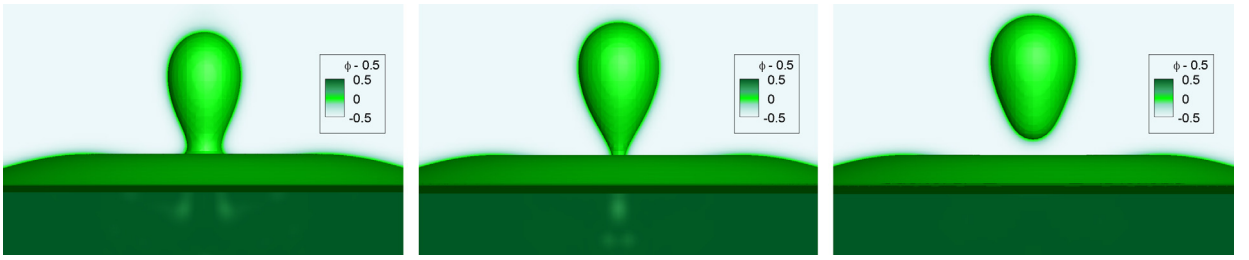

(a) $M = 0.003$ (b) $M = 0.015$ (c) $M = 0.075$

Fig. 13. Effect of the mobility on the pinch-off mechanism at $t^* = 0.8$ ($\rho^* = 1.316$, $\mu^* = 0.5$, $\mathrm{Bo} = 9.59 \times 10^{-2}$, $\mathrm{Oh} = 5.53 \times 10^{-3}$). (a) $\mathrm{Pe} = 75$; (b) $\mathrm{Pe} = 15$; (c) $\mathrm{Pe} = 3$.

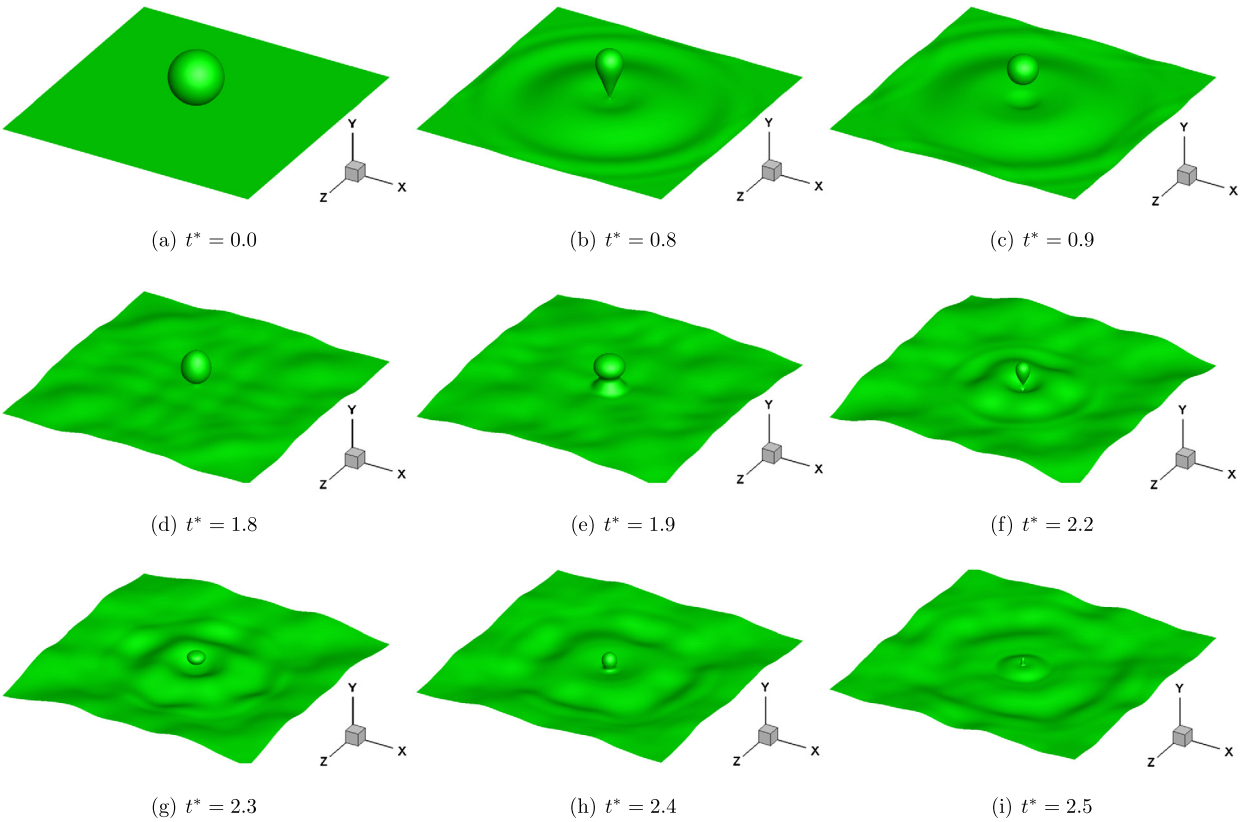

(a) $t^* = 0.0$ (b) $t^* = 0.8$ (c) $t^* = 0.9$

(d) $t^* = 1.8$ (e) $t^* = 1.9$ (f) $t^* = 2.2$

(g) $t^* = 2.3$ (h) $t^* = 2.4$ (i) $t^* = 2.5$

Fig. 14. Coalescence cascade of a liquid drop at a liquid–liquid interface. $\rho^* = 1.316$, $\mu^* = 0.1$, $\mathrm{Bo} = 10^{-2}$, and $\mathrm{Oh} = 10^{-4}$.

In order to see the effect of mobility on the quality of the partial coalescence, we conducted three simulations with the same physical parameters as before but for different mobilities: $M = 0.003$ lu, $M = 0.015$ lu, and $M = 0.075$ lu. The results are shown in Fig. 13. As can be seen in Fig. 13(a), the pinch-off mechanism is arrested when the mobility is the smallest ($M = 0.003$ lu). On the other hand, for the droplet with the highest mobility in Fig. 13(c) the initiation of the partial coalescence is expedited. The intermediate value for the mobility in Fig. 13(b), which was found empirically through trial and error, leads to the best agreement with experimental observations reported by Chen et al. [38].

6.3. Coalescence cascade

We consider one further problem, partial coalescence at a very low Ohnesorge number, where viscous forces are very small relative to inertia and surface tension. We double the grid resolution and increase the drop radius to $R^* = 0.2$. Other dimensionless groups are $\mu^* = 0.1$, $\mathrm{Bo} = 10^{-2}$, and $\mathrm{Oh} = 10^{-4}$. These parameters correspond to extremely low relaxation rates $\tau_L = 0.000015$ lu and $\tau_H = 0.000117$ lu for the light and heavy fluids, respectively, and are chosen to test the stability of the proposed numerical method. With these relaxation rates it is essentially impossible to run a stable simulation using the BGK model or even the standard MRT model on the D3Q27 lattice. At such low Ohnesorge numbers, the droplet undergoes a coalescence cascade [35,36], where partial coalescence occurs multiple times. As can be seen in Fig. 14, the

original drop pinches off at $t^* = 0.8$ creating a daughter droplet that is roughly half the size of the parent drop. The partial coalescence process can now repeat itself as long as the Ohnesorge number of the subsequent daughter droplet remains below a critical value. It has been shown that the cascade process is self-similar in the sense that the ratio of the radius of the daughter droplet to the radius of its parent drop is nearly constant [36]. After bouncing a couple of times, the daughter droplet retouches the liquid–liquid interface, which is now deformed due to reflection of waves from the lateral boundaries, at $t^* = 1.8$. Again, in Fig. 14(e), a capillary wave is created at the exterior surface of the droplet, which leads to another pinch-off mechanism at $t^* = 2.2$. Such a cascade phenomenon has been observed to occur as many as eight times in liquid–liquid experiments [35]. Here though, the second daughter droplet, which is now about one-forth of the original drop, completely merges onto the deformed interface. At $t^* = 2.4$, viscous forces are strong enough to suppress another sequence of the partial coalescence mechanism.

It is worth noting that we also conducted 2D simulations (not shown) for a wide range of Ohnesorge numbers in the search for a pinch-off regime, but partial coalescence was never observed in 2D. This is interesting because there has been some debate as to the mechanism by which the whole process occurs. On the one hand there is a camp that argues that the Rayleigh–Plateau instability is the main mechanism responsible for breakup of the liquid interface [35,36,41], and on the other hand there is a theory by Blanchetti and Bigioni [37], who argued against this mechanism. They claimed that the pinch-off mechanism depends strongly on the inward momentum of the collapsing neck. Our numerical simulations do not support this, but side with postulations based on the Rayleigh–Plateau instability in the pinch-off mechanism of liquid drops. In our 2D simulations, no matter how strong the horizontal momentum of the 2D drop is after the coalescence, pinch-off never occurs. Knowing that the Rayleigh–Plateau instability is essentially a 3D phenomenon and does not trigger in 2D, our simulations tend to support its role and oppose the theory proposed in Ref. [37]. Furthermore, the arguments in Ref. [37] were based on setting the velocity field equal to zero (once the liquid drop had stretched to its maximum height) and restarting the simulations. Aside from this unphysical treatment, it is not clear whether the incompressibility condition was enforced or the pressure field was left intact. Knowing that pressure disturbances in the azimuthal direction are the main mechanisms responsible for Rayleigh–Plateau instability, the conclusions drawn based on this ad hoc treatment is questionable. Moreover, it is not obvious whether simulation of any instability-induced breakup mechanism is possible without introducing a perturbation in the velocity or pressure fields.

7. Summary and conclusion

In this paper we have proposed a novel weighted multiple-relaxation-time lattice Boltzmann method for direct numerical simulation of immiscible fluids. The proposed WMRT–LBM consists of a conservative phase-field LBE for interface tracking and a pressure-evolution LBE, which recovers the Navier–Stokes equations. In addition to its increased numerical stability for the D3Q27 lattice, the proposed WMRT model is shown to be a promising tool for simulation of two-phase flows at very small relaxation times. The WMRT–LBE model was also formulated for utilization on nonuniform grids and equipped with a 3D adaptive mesh refinement algorithm for efficient use of computational resources.

The model was validated by demonstrating that it could faithfully reproduce the dynamics of a rising bubble in a viscous fluid, the bag-breakup mechanism of a falling drop, droplet splashing on a wet surface, and the partial coalescence of a liquid drop at a liquid–liquid interface. At a small enough Ohnesorge number, our simulations of the partial coalescence were found to be in excellent agreement with reported experimental observations. At lower Ohnesorge numbers, we were able to reproduce the so-called coalescence cascade, where a single drop undergoes partial coalescence multiple times. Our numerical simulations further support the idea that the Rayleigh–Plateau instability is responsible for the partial coalescence mechanism. In essence, the proposed WMRT–LBM–AMR was shown to be a successful and reliable model for simulation of breakup and coalescence mechanisms.

Acknowledgements

This material is based upon work supported, fully or in part, by NSF grants EAR-1351625 and EAR-1417264. Any opinions, findings, conclusions, or recommendations do not necessarily reflect the views of the funding agencies.

Appendix A. WMRT for three-dimensional lattices

The moments of the monomials $c_{ix}^l c_{iy}^m c_{iz}^n$ are defined as [8–10,59,46]:

$$\psi_{lmn} = \sum_i c_{ix}^l c_{iy}^m c_{iz}^n \, \bar{g}_i, \tag{A.1}$$

where $\bar{g}_i$ is defined in Eq. (19). For a DdQq model, there exist q independent moments [8–10], and these moments can be orthogonalized in the basis of the monomials in q-dimensional space $\mathbb{R}^q$.

Let $\mathbf{m}_i \in \mathbb{R}^q$ denote a column vector, i.e.,

$$\mathbf{m}_i = (m_{i0}, m_{i1}, \ldots, m_{ib})^\dagger,$$

where $b := q - 1$ is the number of non-zero velocities and † denotes the transpose, thus $\mathbf{m}_i^\dagger$ is a row vector in $\mathbb{R}^q$. The first $1 + d$ independent and orthogonal row vectors are:

$$\mathbf{m}_0^\dagger = (\underbrace{1,\ 1,\ \ldots,\ 1}_{q}),$$
$$\mathbf{m}_1^\dagger = (c_{0x},\ c_{1x},\ c_{2x},\ \ldots,\ c_{bx}),$$
$$\mathbf{m}_2^\dagger = (c_{0y},\ c_{1y},\ c_{2y},\ \ldots,\ c_{by}),$$
$$\mathbf{m}_3^\dagger = (c_{0z},\ c_{1z},\ c_{2z},\ \ldots,\ c_{bz}).$$

By definition these $1 + d$ vectors are orthogonal, i.e., $\mathbf{m}_i^\dagger \cdot \mathbf{m}_j = |\mathbf{m}_i|\,|\mathbf{m}_j|\delta_{ij}$, where $|\mathbf{m}_i|$ is the Euclidean length of the vector $\mathbf{m}_i$ and δ_{ij} is the Kronecker delta. The above $(1 + d)$ vectors correspond to conserved moments in the system, which are the vectors corresponding to the basis of the kernel or the null space of the collision operator. If $\mathbf{g}$ denotes the following vector in $\mathbb{R}^q$,

$$\mathbf{g}(\boldsymbol{x},\ t) = (g_0(\boldsymbol{x},\ t),\ g_1(\boldsymbol{x},\ t),\ \ldots,\ g_b(\boldsymbol{x},\ t))^\dagger,$$

then the conserved moments can be obtained as the following:

$$p = \mathbf{m}_0^\dagger \cdot \mathbf{g} = \mathbf{g}^\dagger \cdot \mathbf{m}_0,$$
$$\rho u_x = \mathbf{m}_1^\dagger \cdot \mathbf{g} = \mathbf{g}^\dagger \cdot \mathbf{m}_1,$$
$$\rho u_y = \mathbf{m}_2^\dagger \cdot \mathbf{g} = \mathbf{g}^\dagger \cdot \mathbf{m}_2,$$
$$\rho u_z = \mathbf{m}_3^\dagger \cdot \mathbf{g} = \mathbf{g}^\dagger \cdot \mathbf{m}_3.$$

The rest of $[q - (1 + d)]$ independent vectors can all be constructed from $\{\mathbf{m}_i | 0 \le i \le d\}$.

For the LB models, the inner product among $\{\mathbf{m}_i\}$ can be defined in two ways, namely with or without the weight coefficients. The most salient difference between the weighted and unweighted orthogonality is certain couplings of moments [14], which may affect the stability of the model. In this work, the inner product is defined with the weights $\{w_i\}$:

$$\langle \mathbf{m}_i,\ \mathbf{m}_j \rangle_w := \sum_{k=0}^{b} w_k m_{ik} m_{jk} \delta_{ij}, \tag{A.2}$$

where m_{ik} and m_{jk} are the kth components of vectors $\mathbf{m}_i$ and $\mathbf{m}_j$, respectively. With $w_k = 1$, the above definition reduces to the usual definition of $\mathbf{m}_i \cdot \mathbf{m}_j$, i.e., the unweighted inner product that is used in standard MRT [10, 46].

With a 3D LB model of q discrete velocities, the first vector in $\mathbb{R}^q$ is the zeroth-order moment, which corresponds to the pressure p in incompressible flows:

$$\mathbf{m}_0 = |\boldsymbol{c}_i|^0 = 1,$$

and the next three vectors in $\mathbb{R}^q$ are the first moments, which correspond to the three components of the flow momentum ρu_x, ρu_y, and ρu_z:

$$\begin{cases} \mathbf{m}_1 = c_{ix}, \\ \mathbf{m}_2 = c_{iy}, \\ \mathbf{m}_3 = c_{iz} \end{cases}$$

The next $(d + 2)(d - 1)/2$ components in $\mathbb{R}^q$ are the second moments, which are related to the shear stress. In 3D, these moments are:

$$\begin{cases} \mathbf{m}_4 = c_{ix} c_{iy}, \\ \mathbf{m}_5 = c_{iy} c_{iz}, \\ \mathbf{m}_6 = c_{iz} c_{ix}, \\ \mathbf{m}_7 = 3c_{ix}^2 - |\boldsymbol{c}_i|^2, \\ \mathbf{m}_8 = c_{iy}^2 - c_{iz}^2 \end{cases}$$

There is another second moment $\mathbf{m}_9 = |\boldsymbol{c}_i|^2 - 1$, which is related to energy, and the rest of the components in $\mathbb{R}^q$ are incrementally higher order non-hydrodynamic moments, which are lattice dependent.

For the D3Q15 lattice

third moment:
$$\begin{cases} \mathbf{m}_{10} = \frac{1}{2} c_{ix} \left(3|\boldsymbol{c}_i|^2 - 5\right), \\ \mathbf{m}_{11} = \frac{1}{2} c_{iy} \left(3|\boldsymbol{c}_i|^2 - 5\right), \\ \mathbf{m}_{12} = \frac{1}{2} c_{iz} \left(3|\boldsymbol{c}_i|^2 - 5\right), \\ \mathbf{m}_{13} = c_{ix} c_{iy} c_{iz} \end{cases}$$

fourth moment:
$$\mathbf{m}_{14} = \frac{1}{2} \left(3|\boldsymbol{c}_i|^4 - 9|\boldsymbol{c}_i|^2 + 4\right)$$

For the D3Q19 lattice

third moments:
$$\begin{cases} \mathbf{m}_{10} = c_{ix} \left(3|\boldsymbol{c}_i|^2 - 5\right), \\ \mathbf{m}_{11} = c_{iy} \left(3|\boldsymbol{c}_i|^2 - 5\right), \\ \mathbf{m}_{12} = c_{iz} \left(3|\boldsymbol{c}_i|^2 - 5\right), \\ \mathbf{m}_{13} = c_{ix} \left(c_{iy}^2 - c_{iz}^2\right), \\ \mathbf{m}_{14} = c_{iy} \left(c_{iz}^2 - c_{ix}^2\right), \\ \mathbf{m}_{15} = c_{iz} \left(c_{ix}^2 - c_{iy}^2\right) \end{cases}$$

fourth moments:
$$\begin{cases} \mathbf{m}_{16} = 3|\boldsymbol{c}_i|^4 - 9|\boldsymbol{c}_i|^2 + 1, \\ \mathbf{m}_{17} = \left(2|\boldsymbol{c}_i|^2 - 3\right) \left(3c_{ix}^2 - |\boldsymbol{c}_i|^2\right), \\ \mathbf{m}_{18} = \left(2|\boldsymbol{c}_i|^2 - 3\right) \left(c_{iy}^2 - c_{iz}^2\right) \end{cases}$$

For the D3Q27 lattice

third moments:
$$\begin{cases} \mathbf{m}_{10} = c_{ix} \left(3|\boldsymbol{c}_i|^2 - 5\right), \\ \mathbf{m}_{11} = c_{iy} \left(3|\boldsymbol{c}_i|^2 - 5\right), \\ \mathbf{m}_{12} = c_{iz} \left(3|\boldsymbol{c}_i|^2 - 5\right), \\ \mathbf{m}_{13} = c_{ix} \left(c_{iy}^2 - c_{iz}^2\right), \\ \mathbf{m}_{14} = c_{iy} \left(c_{iz}^2 - c_{ix}^2\right), \\ \mathbf{m}_{15} = c_{iz} \left(c_{ix}^2 - c_{iy}^2\right), \\ \mathbf{m}_{16} = c_{ix} c_{iy} c_{iz} \end{cases}$$

fourth moments:
$$\begin{cases} \mathbf{m}_{17} = \frac{1}{2} \left(3|\boldsymbol{c}_i|^4 - 9|\boldsymbol{c}_i|^2 + 4\right), \\ \mathbf{m}_{18} = \left(3|\boldsymbol{c}_i|^2 - 4\right) \left(3c_{ix}^2 - |\boldsymbol{c}_i|^2\right), \\ \mathbf{m}_{19} = \left(3|\boldsymbol{c}_i|^2 - 4\right) \left(c_{iy}^2 - c_{iz}^2\right), \\ \mathbf{m}_{20} = c_{ix} c_{iy} \left(3|\boldsymbol{c}_i|^2 - 7\right), \\ \mathbf{m}_{21} = c_{iy} c_{iz} \left(3|\boldsymbol{c}_i|^2 - 7\right), \\ \mathbf{m}_{22} = c_{iz} c_{ix} \left(3|\boldsymbol{c}_i|^2 - 7\right) \end{cases}$$

fifth moments:
$$\begin{cases} \mathbf{m}_{23} = \frac{1}{2} c_{ix} \left(9|\boldsymbol{c}_i|^4 - 33|\boldsymbol{c}_i|^2 + 81\right), \\ \mathbf{m}_{24} = \frac{1}{2} c_{iy} \left(9|\boldsymbol{c}_i|^4 - 33|\boldsymbol{c}_i|^2 + 81\right), \\ \mathbf{m}_{25} = \frac{1}{2} c_{iz} \left(9|\boldsymbol{c}_i|^4 - 33|\boldsymbol{c}_i|^2 + 81\right) \end{cases}$$

sixth moment:
$$\mathbf{m}_{26} = \frac{1}{2} \left(9|\boldsymbol{c}_i|^6 - 18|\boldsymbol{c}_i|^4 + 87|\boldsymbol{c}_i|^2 - 26\right)$$

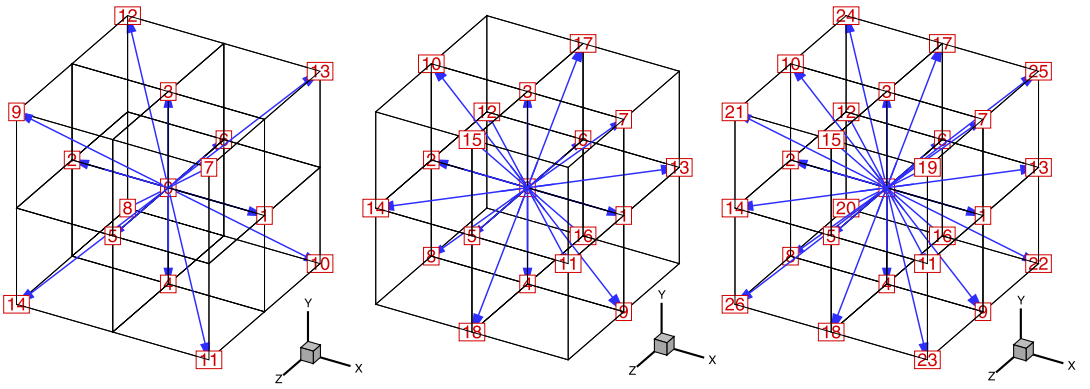

(a) D3Q15 (b) D3Q19 (c) D3Q27

Fig. 15. Discrete velocity sets for 3D LB models.

A.1. D3Q15 model

The discrete velocity set for the D3Q15 is set as is illustrated in Fig. 15(a), and the corresponding weight coefficients are

$$w_i = \frac{1}{72}\begin{cases} 16, & i = 0, \\ 8, & i = 1\text{–}6, \\ 1, & i = 7\text{–}14. \end{cases} \tag{A.3}$$

The weighted transformation matrix $\mathbf{M}$ is given by:

$$\mathbf{M} = \begin{pmatrix} 1 & 1 & 1 & 1 & 1 & 1 & 1 & 1 & 1 & 1 & 1 & 1 & 1 & 1 & 1 \\ 0 & 1 & -1 & 0 & 0 & 0 & 0 & 1 & -1 & -1 & 1 & 1 & -1 & 1 & -1 \\ 0 & 0 & 0 & 1 & -1 & 0 & 0 & 1 & -1 & 1 & -1 & -1 & 1 & 1 & -1 \\ 0 & 0 & 0 & 0 & 0 & 1 & -1 & 1 & -1 & 1 & -1 & 1 & -1 & -1 & 1 \\ 0 & 0 & 0 & 0 & 0 & 0 & 0 & 1 & 1 & -1 & -1 & -1 & -1 & 1 & 1 \\ 0 & 0 & 0 & 0 & 0 & 0 & 0 & 1 & 1 & 1 & 1 & -1 & -1 & -1 & -1 \\ 0 & 0 & 0 & 0 & 0 & 0 & 0 & 1 & 1 & -1 & -1 & 1 & 1 & -1 & -1 \\ 0 & 2 & 2 & -1 & -1 & -1 & -1 & 0 & 0 & 0 & 0 & 0 & 0 & 0 & 0 \\ 0 & 0 & 0 & 1 & 1 & -1 & -1 & 0 & 0 & 0 & 0 & 0 & 0 & 0 & 0 \\ -1 & 0 & 0 & 0 & 0 & 0 & 0 & 2 & 2 & 2 & 2 & 2 & 2 & 2 & 2 \\ 0 & -1 & 1 & 0 & 0 & 0 & 0 & 2 & -2 & -2 & 2 & 2 & -2 & 2 & -2 \\ 0 & 0 & 0 & -1 & 1 & 0 & 0 & 2 & -2 & 2 & -2 & -2 & 2 & 2 & -2 \\ 0 & 0 & 0 & 0 & 0 & -1 & 1 & 2 & -2 & 2 & -2 & 2 & -2 & -2 & 2 \\ 0 & 0 & 0 & 0 & 0 & 0 & 0 & 1 & -1 & -1 & 1 & -1 & 1 & -1 & 1 \\ 2 & -1 & -1 & -1 & -1 & -1 & -1 & 2 & 2 & 2 & 2 & 2 & 2 & 2 & 2 \end{pmatrix} \tag{A.4}$$

Note that the elements in the second, third, and fourth row in $\mathbf{M}$ correspond to the x-, y-, and z-components of the lattice velocity set $\boldsymbol{c}_i$ in units of $c := \delta x/\delta t$. This thus uniquely defines the ordering (or labeling) of the velocity set $\{\boldsymbol{c}_i | 0 \leq i \leq (q-1)\}$ for different lattices.

A.2. D3Q19 lattice

The discrete velocity set for the D3Q19 is set as is illustrated in Fig. 15(b), and the weight coefficients are

$$w_i = \frac{1}{36}\begin{cases} 12, & i = 0, \\ 2, & i = 1\text{–}6, \\ 1, & i = 7\text{–}18. \end{cases} \tag{A.5}$$

The weighted transformation matrix $\mathbf{M}$ is:

$$\mathbf{M} = \begin{pmatrix}
1 & 1 & 1 & 1 & 1 & 1 & 1 & 1 & 1 & 1 & 1 & 1 & 1 & 1 & 1 & 1 & 1 & 1 & 1\\
0 & 1 & -1 & 0 & 0 & 0 & 0 & 1 & -1 & 1 & -1 & 1 & -1 & 1 & -1 & 0 & 0 & 0 & 0\\
0 & 0 & 0 & 1 & -1 & 0 & 0 & 1 & -1 & -1 & 1 & 0 & 0 & 0 & 0 & 1 & -1 & 1 & -1\\
0 & 0 & 0 & 0 & 0 & 1 & -1 & 0 & 0 & 0 & 0 & 1 & -1 & -1 & 1 & 1 & -1 & -1 & 1\\
0 & 0 & 0 & 0 & 0 & 0 & 0 & 1 & 1 & -1 & -1 & 0 & 0 & 0 & 0 & 0 & 0 & 0 & 0\\
0 & 0 & 0 & 0 & 0 & 0 & 0 & 0 & 0 & 0 & 0 & 0 & 0 & 0 & 0 & 1 & 1 & -1 & -1\\
0 & 0 & 0 & 0 & 0 & 0 & 0 & 0 & 0 & 0 & 0 & 1 & 1 & -1 & -1 & 0 & 0 & 0 & 0\\
0 & 2 & 2 & -1 & -1 & -1 & -1 & 1 & 1 & 1 & 1 & 1 & 1 & 1 & 1 & -2 & -2 & -2 & -2\\
0 & 0 & 0 & 1 & 1 & -1 & -1 & 1 & 1 & 1 & 1 & -1 & -1 & -1 & -1 & 0 & 0 & 0 & 0\\
-1 & 0 & 0 & 0 & 0 & 0 & 0 & 1 & 1 & 1 & 1 & 1 & 1 & 1 & 1 & 1 & 1 & 1 & 1\\
0 & -2 & 2 & 0 & 0 & 0 & 0 & 1 & -1 & 1 & -1 & 1 & -1 & 1 & -1 & 0 & 0 & 0 & 0\\
0 & 0 & 0 & -2 & 2 & 0 & 0 & 1 & -1 & -1 & 1 & 0 & 0 & 0 & 0 & 1 & -1 & 1 & -1\\
0 & 0 & 0 & 0 & 0 & -2 & 2 & 0 & 0 & 0 & 0 & 1 & -1 & -1 & 1 & 1 & -1 & -1 & 1\\
0 & 0 & 0 & 0 & 0 & 0 & 0 & 1 & -1 & 1 & -1 & -1 & 1 & -1 & 1 & 0 & 0 & 0 & 0\\
0 & 0 & 0 & 0 & 0 & 0 & 0 & -1 & 1 & 1 & -1 & 0 & 0 & 0 & 0 & 1 & -1 & 1 & -1\\
0 & 0 & 0 & 0 & 0 & 0 & 0 & 0 & 0 & 0 & 0 & 1 & -1 & -1 & 1 & -1 & 1 & 1 & -1\\
1 & -2 & -2 & -2 & -2 & -2 & -2 & 1 & 1 & 1 & 1 & 1 & 1 & 1 & 1 & 1 & 1 & 1 & 1\\
0 & -2 & -2 & 1 & 1 & 1 & 1 & 1 & 1 & 1 & 1 & 1 & 1 & 1 & 1 & -2 & -2 & -2 & -2\\
0 & 0 & 0 & -1 & -1 & 1 & 1 & 1 & 1 & 1 & 1 & -1 & -1 & -1 & -1 & 0 & 0 & 0 & 0
\end{pmatrix} \tag{A.6}$$

A.3. D3Q27 lattice

The discrete velocity set for the D3Q27 is illustrated in Fig. 15(c), and the corresponding weight coefficients are

$$w_i = \frac{1}{216}\begin{cases} 64, & i = 0,\\ 16, & i = 1\text{–}6,\\ 4, & i = 7\text{–}18,\\ 1, & i = 19\text{–}26. \end{cases} \tag{A.7}$$

The weighted transformation matrix $\mathbf{M}$ for the D3Q27 model becomes:

$$\mathbf{M} = \begin{pmatrix}
1 & 1 & 1 & 1 & 1 & 1 & 1 & 1 & 1 & 1 & 1 & 1 & 1 & 1 & 1 & 1 & 1 & 1 & 1 & 1 & 1 & 1 & 1 & 1 & 1 & 1 & 1\\
0 & 1 & -1 & 0 & 0 & 0 & 0 & 1 & -1 & 1 & -1 & 1 & -1 & 1 & -1 & 0 & 0 & 0 & 0 & 1 & -1 & -1 & 1 & 1 & -1 & 1 & -1\\
0 & 0 & 0 & 1 & -1 & 0 & 0 & 1 & -1 & -1 & 1 & 0 & 0 & 0 & 0 & 1 & -1 & 1 & -1 & 1 & -1 & 1 & -1 & -1 & 1 & 1 & -1\\
0 & 0 & 0 & 0 & 0 & 1 & -1 & 0 & 0 & 0 & 0 & 1 & -1 & -1 & 1 & 1 & -1 & -1 & 1 & 1 & -1 & 1 & -1 & 1 & -1 & -1 & 1\\
0 & 0 & 0 & 0 & 0 & 0 & 0 & 1 & 1 & -1 & -1 & 0 & 0 & 0 & 0 & 0 & 0 & 0 & 0 & 1 & 1 & -1 & -1 & -1 & -1 & 1 & 1\\
0 & 0 & 0 & 0 & 0 & 0 & 0 & 0 & 0 & 0 & 0 & 0 & 0 & 0 & 0 & 1 & 1 & -1 & -1 & 1 & 1 & 1 & 1 & -1 & -1 & -1 & -1\\
0 & 0 & 0 & 0 & 0 & 0 & 0 & 0 & 0 & 0 & 0 & 1 & 1 & -1 & -1 & 0 & 0 & 0 & 0 & 1 & 1 & -1 & -1 & 1 & 1 & -1 & -1\\
0 & 2 & 2 & -1 & -1 & -1 & -1 & 1 & 1 & 1 & 1 & 1 & 1 & 1 & 1 & -2 & -2 & -2 & -2 & 0 & 0 & 0 & 0 & 0 & 0 & 0 & 0\\
0 & 0 & 0 & 1 & 1 & -1 & -1 & 1 & 1 & 1 & 1 & -1 & -1 & -1 & -1 & 0 & 0 & 0 & 0 & 0 & 0 & 0 & 0 & 0 & 0 & 0 & 0\\
-1 & 0 & 0 & 0 & 0 & 0 & 0 & 1 & 1 & 1 & 1 & 1 & 1 & 1 & 1 & 1 & 1 & 1 & 1 & 2 & 2 & 2 & 2 & 2 & 2 & 2 & 2\\
0 & -2 & 2 & 0 & 0 & 0 & 0 & 1 & -1 & 1 & -1 & 1 & -1 & 1 & -1 & 0 & 0 & 0 & 0 & 4 & -4 & -4 & 4 & 4 & -4 & 4 & -4\\
0 & 0 & 0 & -2 & 2 & 0 & 0 & 1 & -1 & -1 & 1 & 0 & 0 & 0 & 0 & 1 & -1 & 1 & -1 & 4 & -4 & 4 & -4 & -4 & 4 & -4 & 4\\
0 & 0 & 0 & 0 & 0 & -2 & 2 & 0 & 0 & 0 & 0 & 1 & -1 & -1 & 1 & 1 & -1 & -1 & 1 & 4 & -4 & 4 & -4 & 4 & -4 & -4 & 4\\
0 & 0 & 0 & 0 & 0 & 0 & 0 & 1 & -1 & 1 & -1 & -1 & 1 & -1 & 1 & 0 & 0 & 0 & 0 & 0 & 0 & 0 & 0 & 0 & 0 & 0 & 0\\
0 & 0 & 0 & 0 & 0 & 0 & 0 & -1 & 1 & 1 & -1 & 0 & 0 & 0 & 0 & 1 & -1 & 1 & -1 & 0 & 0 & 0 & 0 & 0 & 0 & 0 & 0\\
0 & 0 & 0 & 0 & 0 & 0 & 0 & 0 & 0 & 0 & 0 & 1 & -1 & -1 & 1 & -1 & 1 & 1 & -1 & 0 & 0 & 0 & 0 & 0 & 0 & 0 & 0\\
0 & 0 & 0 & 0 & 0 & 0 & 0 & 0 & 0 & 0 & 0 & 0 & 0 & 0 & 0 & 0 & 0 & 0 & 0 & 1 & -1 & -1 & 1 & -1 & 1 & -1 & 1\\
1 & -1 & -1 & -1 & -1 & -1 & -1 & 0 & 0 & 0 & 0 & 0 & 0 & 0 & 0 & 0 & 0 & 0 & 0 & 4 & 4 & 4 & 4 & 4 & 4 & 4 & 4\\
0 & -2 & -2 & 1 & 1 & 1 & 1 & 2 & 2 & 2 & 2 & 2 & 2 & 2 & 2 & -4 & -4 & -4 & -4 & 0 & 0 & 0 & 0 & 0 & 0 & 0 & 0\\
0 & 0 & 0 & -1 & -1 & 1 & 1 & 2 & 2 & 2 & 2 & -2 & -2 & -2 & -2 & 0 & 0 & 0 & 0 & 0 & 0 & 0 & 0 & 0 & 0 & 0 & 0\\
0 & 0 & 0 & 0 & 0 & 0 & 0 & -1 & -1 & 1 & 1 & 0 & 0 & 0 & 0 & 0 & 0 & 0 & 0 & 2 & 2 & -2 & -2 & -2 & -2 & 2 & 2\\
0 & 0 & 0 & 0 & 0 & 0 & 0 & 0 & 0 & 0 & 0 & 0 & 0 & 0 & 0 & -1 & -1 & 1 & 1 & 2 & 2 & 2 & 2 & -2 & -2 & -2 & -2\\
0 & 0 & 0 & 0 & 0 & 0 & 0 & 0 & 0 & 0 & 0 & -1 & -1 & 1 & 1 & 0 & 0 & 0 & 0 & 2 & 2 & -2 & -2 & 2 & 2 & -2 & -2\\
0 & 1 & -1 & 0 & 0 & 0 & 0 & -2 & 2 & -2 & 2 & -2 & 2 & -2 & 2 & 0 & 0 & 0 & 0 & 4 & -4 & -4 & 4 & 4 & -4 & 4 & -4\\
0 & 0 & 0 & 1 & -1 & 0 & 0 & -2 & 2 & 2 & -2 & 0 & 0 & 0 & 0 & -2 & 2 & -2 & 2 & 4 & -4 & 4 & -4 & -4 & 4 & 4 & -4\\
0 & 0 & 0 & 0 & 0 & 1 & -1 & 0 & 0 & 0 & 0 & -2 & 2 & 2 & -2 & -2 & 2 & 2 & -2 & 4 & -4 & 4 & -4 & 4 & -4 & -4 & 4\\
-1 & 2 & 2 & 2 & 2 & 2 & 2 & -4 & -4 & -4 & -4 & -4 & -4 & -4 & -4 & -4 & -4 & -4 & -4 & 8 & 8 & 8 & 8 & 8 & 8 & 8 & 8
\end{pmatrix} \tag{A.8}$$

References

[1] A. Prosperetti, G. Tryggvason, Computational Methods for Multiphase Flow, Cambridge University Press, 2009.
[2] J.W. Cahn, J.E. Hilliard, Free energy of a nonuniform system, I: interfacial free energy, J. Chem. Phys. 28 (1958) 258.

[3] S.M. Allen, J.W. Cahn, Mechanisms of phase transformations within the miscibility gap of Fe–rich Fe–Al alloys, Acta Metall. 24 (1976) 425.
[4] S. Chen, G. Doolen, Lattice Boltzmann method for fluid flows, Annu. Rev. Fluid Mech. 30 (1998) 329.
[5] X. He, G.D. Doolen, Thermodynamic foundations of kinetic theory and lattice Boltzmann models for multiphase flows, J. Stat. Phys. 107 (2002) 309.
[6] X. He, L.-S. Luo, A priori derivation of the lattice Boltzmann equation, Phys. Rev. E 55 (1997) R6333–R6336.
[7] X. He, L.-S. Luo, Theory of the lattice Boltzmann method: from the Boltzmann equation to the lattice Boltzmann equation, Phys. Rev. E 56 (1997) 6811.
[8] D. d'Humières, Generalized lattice-Boltzmann equations, in: B.D. Shizgal, D.P. Weave (Eds.), Rarefied Gas Dynamics: Theory and Simulations, Washington, DC, in: AIAA J., vol. 159, 1992, p. 450.
[9] P. Lallemand, L.-S. Luo, Theory of the lattice Boltzmann method: dispersion, dissipation, isotropy, Galilean invariance, and stability, Phys. Rev. E 61 (2000) 6546.
[10] D. d'Humières, I. Ginzburg, M. Krafczyk, P. Lallemand, L.-S. Luo, Multiple-relaxation-time lattice Boltzmann models in three dimensions, Philos. Trans. R. Soc. Lond. A 360 (2002) 437.
[11] Y.H. Qian, D. d'Humièress, P. Lallemand, Lattice BGK models for Navier–Stokes equation, Europhys. Lett. 17 (1992) 479.
[12] H. Chen, S. Chen, H.W. Matthaeus, Recovery of the Navier–Stokes equations using a lattice-gas Boltzmann method, Phys. Rev. A 45 (1992) R5339–R5342.
[13] I. Ginzburg, D. d'Humières, Multireflection boundary conditions for lattice Boltzmann models, Phys. Rev. E 68 (2003) 066614.
[14] P. Dellar, Nonhydrodynamic modes and a priori construction of shallow water lattice Boltzmann equations, Phys. Rev. E 65 (2002) 036309.
[15] M. Geier, M. Schönherr, A. Pasquali, M. Krafczyk, The cumulant lattice Boltzmann equation in three dimensions: theory and validation, Comput. Math. Appl. 70 (2015) 507–547.
[16] M.J. Berger, J. Oliger, Adaptive mesh refinement for hyperbolic partial differential equations, J. Comput. Phys. 53 (1984) 484.
[17] A.M. Khokhlov, Fully threaded tree algorithms for adaptive refinement fluid dynamics simulations, J. Comput. Phys. 143 (1998) 519.
[18] P. MacNeice, K. Olson, C. Mobarry, R. de Fainchtein, C. Packer, PARAMESH: a parallel adaptive mesh refinement community toolkit, Comput. Phys. Commun. 126 (2000) 330.
[19] S. Popinet, Gerris: a tree-based adaptive solver for the incompressible Euler equations in complex geometries, J. Comput. Phys. 190 (2003) 572.
[20] H. Ji, F.-S. Lien, E. Yee, A new adaptive mesh refinement data structure with an application to detonation, J. Comput. Phys. 229 (2010) 8981.
[21] S. Zabelok, R. Arslanbekov, V. Kolobov, Adaptive kinetic-fluid solvers for heterogeneous computing architectures, J. Comput. Phys. 303 (2015) 455–469.
[22] J. Tölke, S. Freudiger, M. Krafczyk, An adaptive scheme using hierarchical grids for lattice Boltzmann multi-phase flow simulations, Comput. Fluids 35 (2006) 820.
[23] Z. Yu, L.-S. Fan, An interaction potential based lattice Boltzmann method with adaptive mesh refinement (AMR) for two-phase flow simulation, J. Comput. Phys. 228 (2009) 6456.
[24] G. Eitel-Amor, M. Meinke, W. Schröder, A lattice-Boltzmann method with hierarchically refined meshes, Comput. Fluids 75 (2013) 127.
[25] M. Hasert, K. Masilamani, S. Zimny, H. Klimach, J. Qi, J. Bernsdorf, S. Roller, Complex fluid simulations with the parallel tree-based lattice Boltzmann solver *Musubi*, J. Comput. Sci. 5 (2014) 784–794.
[26] A. Fakhari, T. Lee, Finite-difference lattice Boltzmann method with a block-structured adaptive-mesh-refinement technique, Phys. Rev. E 89 (2014) 033310.
[27] A. Fakhari, T. Lee, Numerics of the lattice Boltzmann method on nonuniform grids: standard LBM and finite-difference LBM, Comput. Fluids 107 (2015) 205–213.
[28] A. Fakhari, M. Geier, T. Lee, A mass-conserving lattice Boltzmann method with dynamic grid refinement for immiscible two-phase flows, J. Comput. Phys. 315 (2016) 434–457.
[29] M. Geier, A. Fakhari, T. Lee, Conservative phase-field lattice Boltzmann model for interface tracking equation, Phys. Rev. E 91 (2015) 063309.
[30] A. Fakhari, T. Lee, Multiple-relaxation-time lattice Boltzmann method for immiscible fluids at high Reynolds numbers, Phys. Rev. E 87 (2013) 023304.
[31] R. Clift, J.R. Grace, M.E. Weber, Bubbles, Drops, and Particles, Academic Press, New York, 1978.
[32] D. Bhaga, M.E. Weber, Bubbles in viscous liquids: shapes, wakes and velocities, J. Fluid Mech. 105 (1981) 61–85.
[33] N. Baumann, D.D. Joseph, P. Mohr, Y. Renardy, Vortex rings of one fluid in another in free fall, Phys. Fluids A 4 (1992) 567–580.
[34] C. Josserand, S. Zaleski, Droplet splashing on a thin liquid film, Phys. Fluids 15 (2003) 1650.
[35] G.E. Charles, S.G. Mason, The mechanism of partial coalescence of liquid drops at liquid/liquid interfaces, J. Colloid Sci. 15 (1960) 105–122.
[36] S.T. Thoroddsen, K. Takehara, The coalescence cascade of a drop, Phys. Fluids 12 (2000) 1265.
[37] F. Blanchette, T.P. Bigioni, Partial coalescence of drops at liquid interfaces, Nat. Phys. 2 (2006) 254.
[38] X. Chen, S. Mandre, J.J. Feng, Partial coalescence between a drop and a liquid–liquid interface, Phys. Fluids 18 (2006) 051705.
[39] P. Yue, C. Zhou, J.J. Feng, A computational study of the coalescence between a drop and an interface in Newtonian and viscoelastic fluids, Phys. Fluids 18 (2006) 102102.
[40] T. Gilet, K. Mulleners, J.P. Lecomte, N. Vandewalle, S. Dorbolo, Critical parameters for the partial coalescence of a droplet, Phys. Rev. E 75 (2007) 036303.
[41] B. Ray, G. Biswas, A. Sharma, Generation of secondary droplets in coalescence of a drop at a liquid–liquid interface, J. Fluid Mech. 655 (2010) 72–104.
[42] A. Fakhari, M.H. Rahimian, Phase-field modeling by the method of lattice Boltzmann equations, Phys. Rev. E 81 (2010) 036707.
[43] Y. Sun, C. Beckermann, Sharp interface tracking using the phase-field equation, J. Comput. Phys. 220 (2007) 626–653.
[44] P.-H. Chiu, Y.-T. Lin, A conservative phase field method for solving incompressible two-phase flows, J. Comput. Phys. 230 (2011) 185–204.
[45] P.J. Dellar, An interpretation and derivation of the lattice Boltzmann method using Strang splitting, Comput. Math. Appl. 65 (2013) 129–141.
[46] F. Dubois, P. Lallemand, Quartic parameters for acoustic applications of lattice Boltzmann scheme, Comput. Math. Appl. 61 (2011) 3404–3416.
[47] K. Suga, Y. Kuwata, K. Takashima, R. Chikasue, A D3Q27 multiple-relaxation-time lattice Boltzmann method for turbulent flows, Comput. Math. Appl. 69 (2015) 518–529.
[48] Z. Guo, B. Shi, C. Zheng, Chequerboard effects on spurious currents in the lattice Boltzmann equation for two-phase flows, Philos. Trans. R. Soc. Lond. A 369 (2011) 2283–2291.
[49] T. Lee, L. Liu, Lattice Boltzmann simulations of micron-scale drop impact on dry surfaces, J. Comput. Phys. 229 (2010) 8045.
[50] Z. Guo, C. Zheng, B. Shi, Force imbalance in lattice Boltzmann equation for two-phase flows, Phys. Rev. E 83 (2011) 036707.
[51] A. Fakhari, D. Bolster, Diffuse interface modeling of three-phase contact line dynamics on curved boundaries: a lattice Boltzmann model for large density and viscosity ratios, J. Comput. Phys. 334 (2017) 620–638.
[52] D. Lagrava, O. Malaspinas, J. Latt, B. Chopard, Advances in multi-domain lattice Boltzmann grid refinement, J. Comput. Phys. 231 (2012) 4808.
[53] A. Fakhari, M.H. Rahimian, Simulation of an axisymmetric rising bubble by a multiple relaxation time lattice Boltzmann method, Int. J. Mod. Phys. B 23 (2009) 4907–4932.
[54] J. Han, G. Tryggvason, Secondary breakup of axisymmetric liquid drops, I: acceleration by a constant body force, Phys. Fluids 11 (1999) 3650.
[55] A. Fakhari, M.H. Rahimian, Simulation of falling droplet by the lattice Boltzmann method, Commun. Nonlinear Sci. Numer. Simul. 14 (2009) 3046–3055.
[56] M. Jalaal, K. Mehravaran, Fragmentation of falling liquid droplets in bag breakup mode, Int. J. Multiph. Flow 47 (2012) 115–132.
[57] A. Fakhari, M.H. Rahimian, Investigation of deformation and breakup of a falling droplet using a multiple-relaxation-time lattice Boltzmann method, Comput. Fluids 40 (2011) 156–171.
[58] F. Magaletti, F. Picano, M. Chinappi, L. Marino, C.M. Casciola, The sharp-interface limit of the Cahn–Hilliard/Navier–Stokes model for binary fluids, J. Fluid Mech. 714 (2013) 95–126.
[59] B. Dünweg, A.J.C. Ladd, Advanced Computer Simulation Approaches for Soft Matter Sciences III, Springer, Berlin, Heidelberg, 2009, pp. 89–166.